PHYSICAL REVIEW E **70**, 011502 (2004)

Brillouin scattering study of salol: Exploring the effects of rotation-translation coupling

H. P. Zhang, A. Brodin,* H. C. Barshilia,† G. Q. Shen,‡ and H. Z. Cummins
Physics Department, City College of the City University of New York, New York, New York 10031, USA

R. M. Pick
UFR 925, Université Pierre et Marie Curie, Paris, France

(Received 24 December 2003; published 8 July 2004)

Brillouin scattering in liquids composed of optically and mechanically anisotropic molecules is affected by coupling between rotational and translational dynamics. While this effect has been extensively studied in depolarized (VH) scattering where it produces the "Rytov dip," recent theoretical analyses by Pick, Franosch *et al.* show that it should also produce observable effects in polarized (VV) scattering [R. M. Pick *et al.*, Eur. Phys. J. B **31**, 217 (2003); **31**, 229 (2003)]. To test this theory, we carried out Brillouin scattering studies of the molecular glassformer salol in the temperature range 210–380 K, including VH-backscattering, VH-90°, and VV-90° spectra. The data were analyzed consistently to determine the effects of rotation-translation coupling on both the polarized and depolarized spectra. A previously unanticipated feature predicted by these authors was observed: a narrow negative region in the *q*-dependent part of the 90° VV spectra, which we designate as the "VV dip." It is an analog of the Rytov dip observed at high temperatures in the 90° VH spectra, which is also accurately described by this theory. Analysis of the 90° VV spectra was carried out both with and without inclusion of translation-rotation coupling in order to determine quantitatively the role this coupling plays.

DOI: 10.1103/PhysRevE.70.011502 PACS number(s): 64.70.Pf, 78.35.+c, 61.20.Lc

I. INTRODUCTION

In simple liquids composed of isotropic molecules, the polarized (VV) light-scattering spectrum exhibits the familiar Rayleigh-Brillouin triplet due to density fluctuations, while the depolarized (VH) spectrum is much weaker, arising from higher-order processes which also appear weakly in the VV spectra. For liquids of anisotropic molecules there is an additional broad quasielastic component present in both the VV and VH spectra due to orientational dynamics. In the late 1960s, Fabelinskii, Starunov *et al.* [1–4], and Stegeman and Stoicheff [5–7], while studying this orientational component in the VH spectrum of liquids composed of anisotropic molecules, discovered a previously unknown feature—a narrow dip centered at $\omega=0$. The possibility of such a dip had been suggested by Leontovich [8] and Rytov [9] based on concepts of generalized hydrodynamics. Initially, the appearance of the doublet was interpreted as evidence for propagating heavily damped shear modes. However, it was soon recognized that the origin of the "Rytov dip" is rotation-translation (RT) coupling whose most familiar consequence is the flow birefringence of liquids subjected to shear flow [10].

A theoretical analysis based on a two-coupled variable version of the Zwanzig-Mori formalism, which predicts the Rytov dip observed in the high temperature depolarized spectra, was proposed by Andersen and Pecora [11], and by Keyes and Kivelson [12]. In this approach, depolarized light scattering is assumed to originate entirely in the orientational dynamics of the optically anisotropic molecules which is, however, modified by the RT coupling. While the Andersen-Pecora equations were originally derived using the Zwanzig-Mori formalism, Wang showed that, in the small-q limit appropriate to continuum hydrodynamics, they can also be derived phenomenologically if the conventional hydrodynamic equations are extended to include orientational dynamics as well as coupling of orientational motion to shear flow [13,14].

With decreasing temperature, the Rytov dip in the depolarized light scattering spectrum $I_{VH}(\omega)$ narrows and disappears as the broad orientational line narrows; eventually, a pair of symmetrically placed bumps appears on the wings and sharpen into well-defined transverse acoustic modes. This temperature evolution of $I_{VH}(\omega)$ from doublet to singlet to triplet was studied in a series of papers by Wang *et al.* [13–19] who generalized the Andersen-Pecora analysis by explicitly introducing viscoelasticity, i.e., by replacing the shear viscosity constant η_S by a memory function $\eta_S(t)$. However, as Wang noted, a similar viscoelastic generalization should also be included for the other transport coefficients in the dynamical equations [17,19].

Dreyfus and Pick and their co-workers further extended the phenomenological theory of depolarized light scattering by introducing memory functions for all transport coefficients and writing the equation of motion of the orientational variable as a damped oscillator equation rather than a simple relaxation equation. Their approach has been applied to depolarized light scattering studies of the molecular glassformers metatoluidine [20–22] and *ortho*-terphenyl [23,24].

---

*Present address: Experimentalphysik II, Universität Bayreuth, Universitätsstrasse 30, D-95440 Bayreuth, Germany.

†Present address: Surface Engineering Unit, National Aerospace Laboratories, Bangalore 560 017, India.

‡Present address: Center of Laser Applications, University of Tennessee Space Institute, Tullahoma, TN 37388.

While the depolarized spectrum $I_{VH}(\vec{q},\omega)$ is determined by orientational dynamics, the polarized Brillouin spectrum $I_{VV}(\vec{q},\omega)$ and its evolution with temperature primarily reflects the dynamics of longitudinal sound waves with $q \sim 10^5\ \mathrm{cm}^{-1}$ and their interaction with structural relaxation. Typically, for liquids of isotropic molecules, as T decreases from above the melting temperature T_m to below the glass-transition temperature T_g, the Brillouin linewidth $\Delta\omega_B$ first increases, passes through a maximum, and then decreases again, while the Brillouin peak position ω_B shifts monotonically to higher frequencies. The increase in ω_B occurs predominantly in the temperature range where $\Delta\omega_B$ is largest. As this temperature evolution occurs, another central component (the Mountain mode) appears, centered at $\omega=0$, and narrows as T decreases, eventually disappearing inside of the instrumental resolution function.

However, as recognized by Dreyfus *et al.* [21], Wang and Zhang [17], and Chappell and Kivelson [25], RT coupling should also affect the polarized light scattering spectrum, because the longitudinal flow (or uniaxial strain) characterizing longitudinal acoustic modes is a superposition of pure compression and shear. Approximate expressions for the polarized spectrum $I_{VV}(\vec{q},\omega)$ including RT coupling were given in Refs. [17,19,21], but have not been tested experimentally. Instead, polarized Brillouin spectra have been analyzed ignoring RT coupling, assuming that the orientational mode is simply added to a typical density fluctuation spectrum $I_{VV}(\vec{q},\omega)$ appropriate for a liquid of isotropic molecules. Structural relaxation effects are usually incorporated in a frequency-dependent longitudinal viscosity $\eta_L(\omega)$ which also explains the Mountain mode.

Recently, Pick, Dreyfus, Franosch, and Latz, have undertaken a unified analysis of polarized and depolarized light scattering spectra using both a phenomenological analysis [21,26], and a microscopic Zwanzig-Mori approach [27]. Their analysis provides a consistent theory of both spectra that includes all the effects of RT coupling and viscoelasticity. The light-scattering investigation of salol reported here was undertaken primarily to see if the spectra of this much-studied molecular glassforming liquid could be successfully analyzed using this new formulation, and, in particular, to see if the predicted effects of RT coupling on the polarized spectra could be unambiguously demonstrated. As we will show, the theory is able to consistently describe our three sets of spectra: $I_{VH}^{back}(\omega)$, $I_{VH}^{90}(\vec{q},\omega)$, and $I_{VV}^{90}(\vec{q},\omega)$. In particular, we looked for—and observed—the new effect predicted by these papers: a "VV-dip" feature in the q-dependent part of the $I_{VV}(\vec{q},\omega)$ spectrum which becomes negative at high temperatures and low frequencies. (A brief discussion of this new I_{VV} effect was reported in Ref. [28].)

In carrying out our data analysis, we will not make explicit use of the mode coupling theory (MCT) [29]. However, in the spirit of MCT, we will use a form for the memory functions that combines a Cole-Davidson (CD) function for the α peak with a power-law term $B\omega^a$ to represent the high-frequency "fast β" relaxation. This "hybrid model," which has been used in several previous light-scattering studies, incorporates the main characteristics of correlation (or relaxation) functions predicted by MCT in the frequency range of Brillouin scattering experiments.

A major problem that arises in carrying out tests of the theory is the presence of a large number of material-dependent parameters. Generally, fits of experimental data to theoretical models become less meaningful as the number of free parameters increases, especially if there are few well-defined features (e.g., peaks) in the data. We therefore organize our data analysis to have four free parameters at most. First, we use existing literature values wherever possible (e.g., viscosity, density, sound velocity). We analyze the depolarized backscattering spectra first to determine the parameters of the pure orientational dynamics, and then fix these in analyzing the 90° depolarized spectra. Finally, with the parameters of the orientational and shear dynamics fixed, we analyze the 90° polarized spectra with only three free fitting parameters.

This analysis is also relevant to the ongoing effort to fully understand the dynamics of the liquid-glass transition. The fundamental quantitative theory of this transition is MCT which is primarily a microscopic theory of density fluctuation dynamics. Often, however, experimental data that is compared to MCT predictions primarily reflects orientational dynamics (as in our depolarized salol spectra). Thus, a detailed understanding of the interaction between orientational and translational dynamics should be included in the comparison of such data with MCT.

II. THEORY

A. Hydrodynamics

Light scattering by simple liquids composed of isotropic molecules is primarily due to long-wavelength density fluctuations whose dynamics are determined by the classical equations of continuum hydrodynamics (c.f., Ref. [30]). The relevant continuum quantities, averaged over a volume element large enough to contain many molecules but small compared to the wavelength of light, are the mass density $\rho(\vec{r},t)$, the velocity $\vec{V}(\vec{r},t)$, and the temperature $T(\vec{r},t)$. However, we assume that the time window of interest is short enough so that fluctuations in T can be ignored.

For a liquid composed of anisotropic molecules, an additional nonhydrodynamic variable is required to describe the departure from isotropy of the average molecular orientation within a small volume element. For linear (or axially symmetric) molecules, if $P(\theta,\phi,\vec{r},t)$ is the probability density of finding a molecule at $\vec{r}$ with its axis $\hat{\mu}$ pointing in the direction (θ,ϕ), an appropriate variable is the orientational density,

$$Q_{ij}(\vec{r},t) = \int \sin\,\theta d\theta d\phi P(\theta,\phi,\vec{r},t) C_{ij}[\hat{u}(\theta,\phi)] \tag{1}$$

with $C_{ij}[\hat{u}(\theta,\phi)]=\left[\hat{u}_i(\theta,\phi)\hat{u}_j(\theta,\phi)-\frac{1}{3}\delta_{ij}\right]$, which forms a symmetric traceless second-rank tensor $\bar{\bar{Q}}$. The orientational variable is often treated as being independent of the hydrodynamic variables. However, as noted in the Introduction, there is an interaction between $\bar{\bar{Q}}$ and the strain rate $\bar{\bar{\tau}}$ (RT coupling) which causes mechanically anisotropic molecules to preferentially orient with their long axes in the direction of flow. Consequently, the equations of motion for $\bar{\bar{Q}}$ and for the stress tensor $\bar{\bar{\sigma}}$ will include cross terms.

In order to generalize the hydrodynamic equations to include $\bar{\bar{Q}}$, one needs to construct an equation of motion for $\bar{\bar{Q}}$ and also to modify $\bar{\bar{\sigma}}$ to include coupling between Q_{ij} and τ_{ij}. This generalization has been reviewed in detail by Dreyfus *et al.* [21] and will be described briefly here.

For the equation of motion of $\bar{\bar{Q}}$, Dreyfus *et al.* used a damped harmonic oscillator equation:

$$\frac{\partial^2}{\partial t^2}Q_{ij} = -\omega_R^2 Q_{ij} - \Gamma\frac{\partial}{\partial t}Q_{ij} + \Lambda'\mu\tau_{ij}, \tag{2}$$

where ω_R is a libration frequency, Γ is the orientational friction coefficient, and the last term incorporates the coupling of orientation to shear flow. For the modified stress tensor, they write:

$$\bar{\bar{\sigma}} = (-p + \eta_B\vec{\nabla}\cdot\vec{V})\bar{\bar{I}} + \eta_S\bar{\bar{\tau}} - \mu\frac{\partial}{\partial t}\bar{\bar{Q}} \tag{3}$$

(where p is the pressure, η_B and η_S are the bulk and shear viscosities, μ is the RT coupling constant, and $\bar{\bar{I}}$ is a unit tensor). For the off-diagonal components (e.g., σ_{yz} with $\vec{V}=V_y\hat{y}$), Eq. (3) becomes

$$\sigma_{yz} = \eta_S\frac{\partial V_y}{\partial z} - \mu\frac{\partial}{\partial t}Q_{yz}. \tag{4}$$

When dealing with supercooled liquids, the previous equations need to be generalized to include retardation effects. The shear viscosity contribution to the σ_{yz} stress tensor component, $\eta_S(\partial V_y/dz)$, for example, can be generalized to

$$\sigma_{yz} = \int_0^t \eta_S(t-t')\frac{dV_y(t')}{dz}dt' \equiv \eta_S \otimes \frac{dV_y}{dz}, \tag{5}$$

where $\eta_S(t-t')$ is a memory function and the symbol $\otimes$ stands for convolution. In the treatment of Dreyfus *et al.*, all transport coefficients are generalized in this way. With this generalization, the coupled equations of motion for $\vec{J}$ (the momentum density) and $\bar{\bar{Q}}$ are

$$\frac{\partial}{\partial t}\vec{J}(\vec{r},t) = \vec{\nabla}\cdot\bar{\bar{\sigma}}(\vec{r},t), \tag{6}$$

$$\bar{\bar{\sigma}} = (-p + \eta_B \otimes \vec{\nabla}\cdot\vec{V})\bar{\bar{I}} + \eta_S \otimes \bar{\bar{\tau}} - \mu \otimes \frac{\partial}{\partial t}\bar{\bar{Q}}, \tag{7}$$

$$\frac{\partial^2}{\partial t^2}\bar{\bar{Q}} = -\omega_R^2\bar{\bar{Q}} - \Gamma \otimes \frac{\partial}{\partial t}\bar{\bar{Q}} + \Lambda'\mu \otimes \bar{\bar{\tau}}. \tag{8}$$

In the following analysis, these equations will be linearized, assuming small fluctuations around equilibrium.

B. Light scattering

To analyze the light scattering spectra, we will follow the scattering geometry *I* notation of Berne and Pecora where both the incident ($\vec{k}_i$) and scattered ($\vec{k}_f$) wave vectors are in the *xz* plane [31]. The scattering vector $\vec{q}=\vec{k}_i-\vec{k}_f$ is in the $-\vec{z}$ direction while the polarization (V) of the incident light is along $\vec{y}$. The scattered electric field amplitude $E^f(t)$ is related to $\hat{e}_i$ and $\hat{e}_f$, the unit polarization vectors of the incident and scattered light and to $\delta\bar{\bar{\epsilon}}$, the fluctuation of the dielectric tensor, by

$$E^f(\vec{r},t) = A\hat{e}_f\cdot\delta\bar{\bar{\epsilon}}(\vec{r},t)\cdot\hat{e}_i, \tag{9}$$

where the constant A is proportional to the incident field amplitude E^i, the sample volume, and the collection solid angle.

For VV scattering, the polarization of the scattered light is along $\vec{y}$; for VH scattering it is in the *xz* plane and fluctuations in both ϵ_{xy} and ϵ_{yz} contribute to the scattering. The scattered field amplitudes are

$$E^f_{VV}(\vec{r},t) = A\delta\epsilon_{yy}(\vec{r},t), \tag{10a}$$

$$E^f_{VH}(\vec{r},t) = A\left[\delta\epsilon_{xy}(\vec{r},t)\sin\left(\frac{\theta}{2}\right) - \delta\epsilon_{yz}(\vec{r},t)\cos\left(\frac{\theta}{2}\right)\right]. \tag{10b}$$

(Note that in the publications of Dreyfus *et al.*, $\epsilon_{yy}=\epsilon_{\perp\perp}$, $\epsilon_{yz}=\epsilon_{\perp\parallel}$, and $\epsilon_{xy}=\epsilon_{\perp\perp'}$.) From symmetry considerations,

$$\delta\bar{\bar{\epsilon}}(\vec{r},t) = a\,\delta\rho(\vec{r},t)\bar{\bar{I}} + b\bar{\bar{Q}}(\vec{r},t) \tag{11}$$

(where a and b are material-dependent constants), so that the diagonal elements of $\bar{\bar{\epsilon}}$ can couple to fluctuations in both density and orientation, while the off-diagonal elements couple only to orientation.

From the Wiener-Khintchine theorem, the power spectrum of the scattered light is given by the real part of the Fourier transform in space ($e^{i\vec{q}\cdot\vec{r}}$) and in time ($e^{-i\omega t}$) of the autocorrelation function of the scattered field amplitude $E^f(\vec{r},t)$:

$$I(\vec{q},\omega) = \frac{1}{2\pi}\mathrm{Re}\int d^3r'\int_0^\infty dt'\langle E^f(\vec{r}+\vec{r}',t+t') \times E^f(\vec{r},t)\rangle\exp[i(\vec{q}\cdot\vec{r}'-\omega t')], \tag{12}$$

where $\langle\cdots\rangle$ implies an average over $\vec{r}$ and t.

From Eqs. (10)–(12), we see that the depolarized spectrum $I_{VH}(\vec{q},\omega)$ involves only two correlation functions since Q_{xy} and Q_{yz} are uncorrelated: $\langle Q_{xy}(\vec{q},t)Q_{xy}(\vec{q},0)\rangle$ and $\langle Q_{yz}(\vec{q},t)Q_{yz}(\vec{q},0)\rangle$. The polarized spectrum, $I_{VV}(\vec{q},\omega)$, involves four correlation functions: $\langle\delta\rho(\vec{q},t)\delta\rho(\vec{q},0)\rangle$, $\langle Q_{yy}(\vec{q},t)Q_{yy}(\vec{q},0)\rangle$, $\langle\delta\rho(\vec{q},t)Q_{yy}(\vec{q},0)\rangle$, and $\langle Q_{yy}(\vec{q},t)\delta\rho(\vec{q},0)\rangle$.

Calculation of the spectra $I_{VH}(\vec{q},\omega)$ and $I_{VV}(\vec{q},\omega)$, starting from Eq. (12), has been carried out in Refs. [21,26], using the Laplace transform convention:

$$F(\omega) = \mathrm{LT}[f(t)] = i\int_0^\infty dt\ f(t)e^{-i\omega t} \tag{13}$$

with the results given below.

C. The depolarized light scattering spectrum $I_{VH}(\vec{q},\omega)$

The calculation described in Ref. [21] yields

$$I_{VH}(\vec{q},\omega) = \frac{A^2}{\omega}\mathrm{Im}\left\{ b^2\left[1-\frac{\omega_R^2}{D(\omega)}\right] + \frac{\rho_m}{\Lambda'}(\omega_R q)^2\cos^2\left(\frac{\theta}{2}\right) \times\left[\frac{\Lambda'}{\rho_m}br(\omega)\right]^2 P_T(\vec{q},\omega)\right\}\langle|Q_{xy}|^2\rangle, \tag{14}$$

where $\rho_m = \langle\rho(\vec{r},t)\rangle$,

$$D(\omega) = \omega_R^2 + \omega\Gamma(\omega) - \omega^2, \tag{15}$$

$$r(\omega) = \omega\mu(\omega)[D(\omega)]^{-1}, \tag{16}$$

$P_T(\vec{q},\omega)$, the transverse propagator, is

$$P_T(\vec{q},\omega) = \left[\omega^2 - \frac{q^2}{\rho_m}[\omega\eta_S(\omega) - \Lambda' r^2(\omega)D(\omega)]\right]^{-1} = \left[\omega^2 - \frac{q^2}{\rho_m}[\omega\eta_T(\omega)]\right]^{-1} \tag{17}$$

and $\langle|Q_{xy}|^2\rangle$ is the $\vec{q}\to 0$ limit of $\langle Q_{xy}(\vec{q},0)Q_{xy}(\vec{q},0)\rangle$. $\eta_T(\omega)$, defined in Eq. (17), is the transverse viscosity which is the shear viscosity $\eta_S(\omega)$ renormalized by the RT coupling.

The first term in Eq. (14) represents the pure orientational spectrum and is independent of q. The second term is the product of two factors: $P_T(\vec{q},\omega)$ which is the propagator for a transverse excitation with wave vector q, and $[(\Lambda'/\rho_m)br(\omega)]^2$ which couples the excitation to the orientation of molecules via RT coupling. [Note that $r(\omega)$ is proportional to $\mu(\omega)$.]

With the abbreviation $A^2b^2\langle|Q_{xy}|^2\rangle = I_0$, and defining $R_1(\vec{q},\omega)$ and $R(\omega)$ as

$$R_1(\vec{q},\omega) = \frac{\rho_m}{\Lambda'}(\omega_R q)^2\left[\frac{\Lambda'}{\rho_m}r(\omega)\right]^2 P_T(\vec{q},\omega) \tag{18}$$

and

$$R(\omega) = \left[1 - \frac{\omega_R^2}{D(\omega)}\right], \tag{19}$$

the depolarized light-scattering spectrum can be expressed as

$$I_{VH}(\vec{q},\omega) = \frac{I_0}{\omega}\mathrm{Im}\left[R(\omega) + R_1(\vec{q},\omega)\cos^2\left(\frac{\theta}{2}\right)\right] \tag{20}$$

Equation (20) is the form used by Dreyfus *et al.* to analyze depolarized light-scattering spectra of metatoluidine [20–22]. If viscoelastic effects are ignored (which is appropriate at high temperatures), and $R(\omega)$ is assumed to be a Lorentzian, the $I_{VH}(\vec{q},\omega)$ spectrum predicted by Eq. (14) reduces to the spectrum of Andersen and Pecora [11] as shown in Ref. [21].

D. The polarized light scattering spectrum $I_{VV}(\vec{q},\omega)$

The calculation of $I_{VV}(\vec{q},\omega)$ is described in detail by Pick *et al.* [26]. The result of the (lengthy) calculation is

$$I_{VV}(\vec{q},\omega) = \frac{A^2}{\omega}\mathrm{Im}\left\{\frac{4b^2}{3}\left[1-\frac{\omega_R^2}{D(\omega)}\right] + \frac{\rho_m}{\Lambda'}(\omega_R q)^2 \times\left[a + \frac{2\Lambda'}{3\rho_m}br(\omega)\right]^2 P_L(\vec{q},\omega)\right\}\langle|Q_{xy}|^2\rangle, \tag{21}$$

where $P_L(\vec{q},\omega)$, the longitudinal phonon propagator, is given by

$$P_L(\vec{q},\omega) = \left[\omega^2 - \frac{q^2}{\rho_m}[\rho_m C_0^2 + \omega\eta_L(\omega)]\right]^{-1}, \tag{22}$$

where C_0 is the adiabatic sound velocity, and $\eta_L(\omega)$, the frequency-dependent longitudinal viscosity, is

$$\eta_L(\omega) = \eta_B(\omega) + \frac{4}{3}\eta_T(\omega). \tag{23}$$

Note that—as in the VH case—RT coupling enters Eq. (21) twice. First, in the longitudinal propagator $P_L(q,\omega)$, and again, in the last square brackets where the coupling of the longitudinal sound wave to orientation provides a second channel for light scattering.

E. Zwanzig-Mori analysis

In constructing the phenomenological theory, there is some ambiguity in the choice of the terms in the equations of motion. A microscopic theory based on the Zwanzig-Mori projection operator formalism can eliminate these ambiguities and can also provide microscopic expressions for the phenomenological coupling constants. A very general microscopic theory was given by Franosch, Fuchs, and Latz [32]. Introducing the orientational tensor and its time derivative as additional variables of the problem, Letz and Latz [33] showed that the Zwanzig-Mori formalism was able to justify the phenomenological equations of Ref. [21]. Later, Franosch *et al.* [27] reformulated the microscopic analysis, deriving expressions for the spectra with the same structure as those obtained with the phenomenological theory. The set of selected variables used in their calculation was ρ, $\vec{J}$, $\bar{\bar{Q}}$, and $(\partial/\partial t)\bar{\bar{Q}}$. Their analysis showed that Eqs. (14) and (21) for $I_{VV}(\vec{q},\omega)$ and $I_{VH}(\vec{q},\omega)$ are exact. Also, the relevant memory functions were found to have well-behaved long-time behavior, allowing the use of simple modeling functions. It is also possible to show, within this formalism, that if general molecular shape is included (rather than requiring axial symmetry), the same equations are obtained for the spectra although the microscopic definitions of the memory kernels have to be modified [34].

We note that in the Zwanzig-Mori approach for simple liquids, both ρ and $\vec{J}$ must be included to obtain propagating wave solutions for $\rho_q(t)$. Similarly, both $\bar{\bar{Q}}$ and $(\partial/\partial t)\bar{\bar{Q}}$ are required to obtain the oscillatory solutions of Eq. (2). If $(\partial/\partial t)\bar{\bar{Q}}$ is not included, the equation of motion for $\bar{\bar{Q}}$ will be relaxational, and the corresponding memory functions not properly behaved at long times [27].

TABLE I. Properties of Salol. (Salol, Phenyl Salicylate; Benzoic acid 2-hydroxy phenyl ester).

Property	Value
Formula	$C_{13}H_{10}O_3$
Molecular Weight	214.21
Melting Temperature T_m	316 K (43 °C)
Boiling Point T_b	446 K (173 °C)
Glass Transition T_g	$\sim$218 K (−55 °C)
Density (g/cm^3)	$\rho_m = 1.4516 - 8.57 \times 10^{-4}$ T (K)[a]
Refractive Index	$n = 1.718 - 4.321 \times 10^{-4}$ T (K)[a]
Viscosity	$\eta_S(T)$[b]
Sound Velocity ($\omega \rightarrow 0$)	$C_0 = 2448 - 3.23$ T (m/sec)[c]
T_C (MCT crossover T)	256 ± 5 K[d]; 253 ± 4 K[e]; 266 K[f] 250 ± 5 K[g]
λ (MCT exponent parameter)	0.70[d]; 0.73[e,g]

[a] From Ref. [7].
[b] From Refs. [46–48]
[c] From Ref. [37]
[d] From Ref. [35] *I*-MCT
[e] From Ref. [53] OKE
[f] From Ref. [64] [time-resolved]
[g] From Ref. [65] *E*-MCT

III. EXPERIMENTS

Salol (phenyl salicylate, melting temperature $T_m = 316$ K, glass-transition temperature $T_g \sim 218$ K) is a fragile molecular glassforming material that supercools easily. It has been studied extensively with a wide range of experimental techniques, so a great deal of information is available for comparison with new experimental studies and analyses. Experiments in which the depolarized backscattering spectra of salol were compared with predictions of the mode coupling theory indicated that T_C, the crossover temperature of MCT, is $T_C = 256 \pm 5$ K [35]. Some of the relevant properties of salol are collected in Table I.

There have been several previous polarized and depolarized Brillouin scattering studies of salol. The evolution of the VH spectrum from a high-temperature doublet to a low-temperature triplet was studied by Fabelinskii *et al.* [2–4], Vaucamps *et al.* [36], Enright and Stoicheff [7], and Wang and Zhang [17]. The VV spectrum was studied by Wang and Zhang [17] and by Dreyfus *et al.* [37]. The results of these experiments will be compared with ours in Sec. VII A.

The total depolarized light-scattering cross section of salol was previously measured and compared with the estimated value for dipole-induced-dipole scattering, the major nonorientational contribution to the total intensity [38]. The results indicated that orientational dynamics account for approximately 97% of the total scattered intensity, justifying the use for salol of the theories discussed in Sec. II in which depolarized scattering due to mechanisms other than orientational dynamics is ignored.

A. Sample preparation

Salol samples for our light-scattering experiments were prepared by triple vacuum distillation of phenyl salicylate purchased from Sigma Chemical Company. The final distillation was made into cylindrical glass sample cells which were then flame sealed under vacuum. The sample was mounted in a copper housing on the cold finger of an Oxford LN2 cold-finger cryostat with an ITC-4 temperature controller connected to a Pt resistance thermometer attached near the top of the cold finger. Liquid Gallium-Indium alloy was used to provide thermal contact between the sample cell and the bottom of the copper housing. For the photon correlation spectroscopy (PCS) experiments, to have more precise temperature readings, a second platinum resistance thermometer was attached to the bottom of the copper housing close to the sample and was monitored with an Omega RTD digital thermometer. The readings obtained with this second thermometer were $\sim$1 K higher than the first thermometer, indicating a small temperature gradient in the cryostat. Brillouin, Raman, and photon correlation experiments were carried out with the same sample and cryostat to maintain consistency in the temperature measurements.

B. Brillouin and Raman scattering

The Brillouin scattering experiments were performed with incident 514.5 nm monomode laser excitation of $\sim$250 mW; the spectra were measured with a Sandercock six-pass tandem Fabry-Perot interferometer in the range 0.3–40 GHz. A 1024 channel multiscaler was used to collect the data with 1.0 ms dwell time per channel ($\sim$1 sec per scan). Between 2000 and 6000 scans were accumulated, depending on the scattered intensity. At each temperature, both VV and VH 90° spectra were recorded as well as VH 173° near-backscattering spectra. After changing T, the cryostat was allowed to restabilize for at least one-half hour before recording spectra. During the experiment, an instrument function was recorded which was convoluted with theoretical functions in the fit procedures.

To extend the VH 173° near-backscattering spectra to higher frequencies for the analysis of the orientational function $R(\omega)$, Raman scattering spectra were obtained with a Spex 1401 tandem grating spectrometer with the slit widths set to a 55 GHz bandpass. The 488 nm multimode output from a Coherent Innova-80 Argon laser provided $\sim$75 mW at the sample. Raman spectra were accumulated in 90° H(V+H) geometry, taking $\sim$30 minutes per run. (At frequencies in the Raman range, these spectra and VH backscattering spectra are indistinguishable.) The combined interferometric + Raman VH 173° spectra are shown in Fig. 1.

These spectra, converted to susceptibility spectra $\chi''(\omega)$ by dividing by the Bose factor, are shown in the next section in Fig. 9. The complete set of susceptibility spectra was normalized to optimize overlap in the 1.5–2.0 THz region. The 90° VH and VV spectra for the temperature range 210–380 K are shown in Figs. 2 and 3.

C. Photon correlation spectroscopy

Photon correlation spectra were obtained at temperatures of 221.8, 224.4, 226.4 231.3, 236.1, 241.3, and 246.1 K with a scattering angle of 90°. 488 nm incident laser light from a

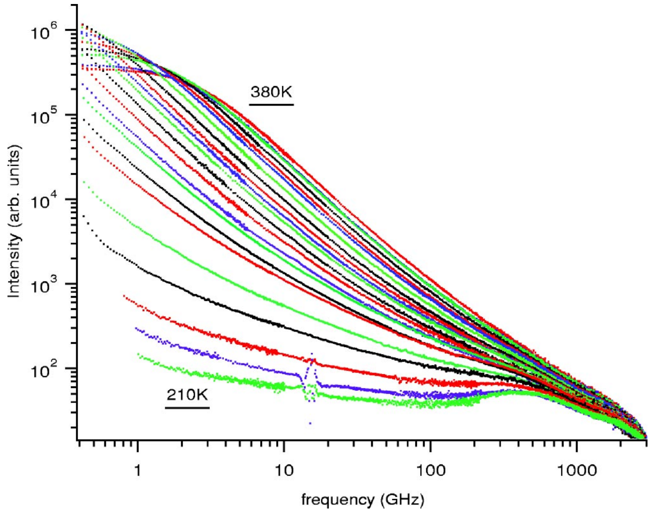

FIG. 1. (Color online) Salol $I_{VH}(\omega)$ backscattering spectra; $T=210$, 220, 230, 240, 250, 255, 260, 265, 270, 275, 280, 285, 290, 295, 300, 310, 320, 330, 340, 350, 360, 370, and 380 K.

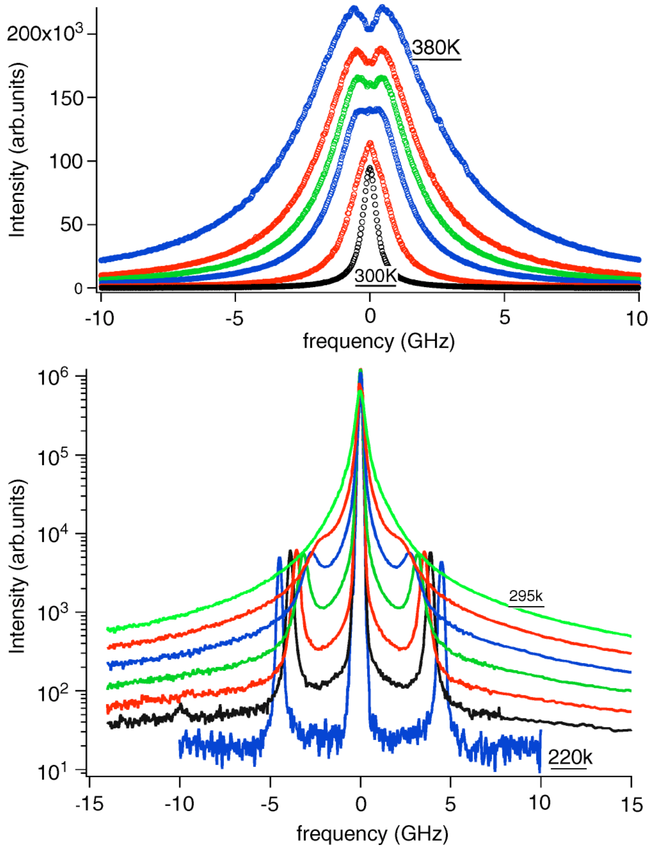

FIG. 2. (Color online) Salol $I_{VH}^{90}(\omega)$ spectra (selected subset of temperatures shown in Fig. 1). Includes vertical shifts for clarity. Upper panel (linear axis): $T=380$, 360, 350, 340, 320, and 300 K, illustrating change from high-T "doublet" with Rytov dip to intermediate temperature single orientational line at 320 K. Lower panel (log axis): $T=295$, 280, 270, 260, 250, 240, and 220 K, illustrating appearance at ~280 K of weak TA modes which sharpen with decreasing T.

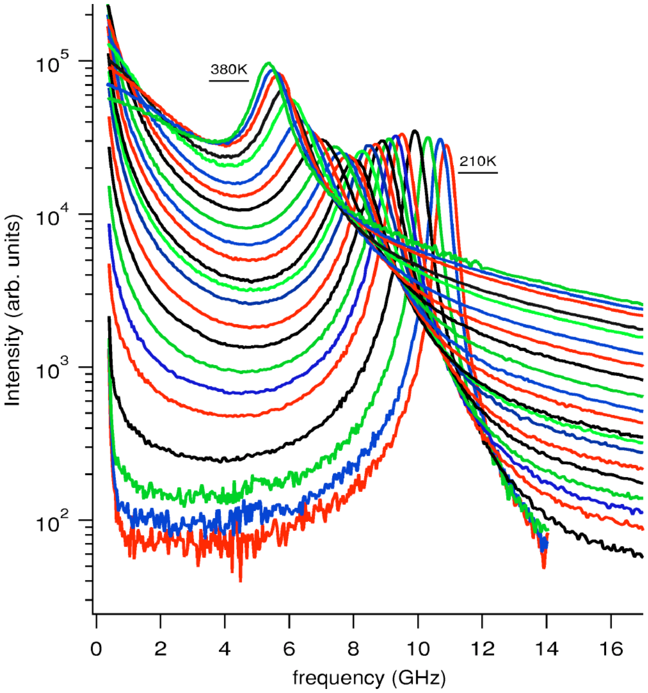

FIG. 3. (Color online) Salol $I_{VV}^{90}(\omega)$ spectra (Stokes side only) at the same 23 temperatures as in Fig. 1.

Spectra-Physics argon laser provided ~20 mW of single-mode power at the sample. The incident light was vertically polarized, and horizontal polarization was selected for the scattered light (VH). Correlation data were accumulated for 5–10 min with count rates of 5–10 kcts/sec. At the lowest temperature, 20 min runs were necessary. The normalized correlation functions $C(t)/B$, where the background $B=C(t\rightarrow\infty)$, are shown with the Kohlrausch-Williams-Watts (KWW) fits in Fig. 4.

D. The relaxation time $\tau_\alpha(T)$

The PCS data were fit to the KWW expression:

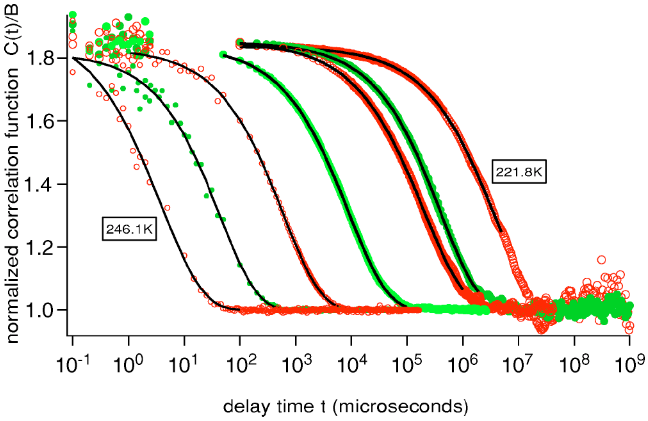

FIG. 4. (Color online) Normalized photon correlation spectra for 90° VH scattering. T (from left to right): 246.1, 241.3, 236.1, 231.3, 226.4, 224.4, and 221.8 K. Solid lines are KWW fits described in the text.

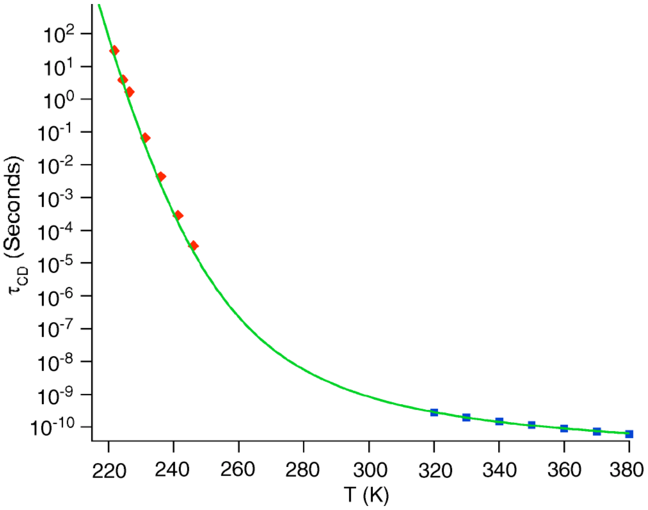

FIG. 5. (Color online) Orientational $\tau_R(T)$. Squares: τ_R from Cole-Davidson fits to high-temperature VH backscattering spectra. Diamonds: τ_R from KWW fits to low-temperature 90° VH PCS spectra. The line is a fit of the data to Eq. (27) with $A=-11.05$, $B=234.81$, $C=6.185$, and $T_0=248.44$ K.

$$C(t)/B = 1 + a\ \exp[-2(t/\tau_K)^{\beta_K}]. \tag{24}$$

The amplitude factor a obtained in the fits was ~ 0.85, indicating that in this temperature range the α decay begins from a plateau level $f_q = \sqrt{a} \sim 0.92$, preceded by a fast relaxation process too fast to appear in the PCS time window. The τ_K and β_K values obtained from the fits were averaged over several runs for each temperature and converted to the corresponding Cole-Davidson values as described by Lindsey and Patterson [39]. The resulting low-temperature τ_R values are plotted in Fig. 5. The overall average β_K value was 0.625, for which $\beta_R=0.50$.

At high temperatures, τ_R can be found from the depolarized backscattering spectrum which, from Eq. (20), is given by

$$I_{VH}^{back}(\omega) = \frac{I_0}{\omega} \mathrm{Im}\ R(\omega). \tag{25}$$

The α-relaxation region of $R(\omega)$ can be modeled by a Cole-Davidson function:

$$R(\omega) = R_0[1 - (1 + i\omega\tau_R)^{-\beta_R}]. \tag{26}$$

The susceptibility spectra $\chi''(\omega)$, which are $\propto R''(\omega)$, are shown in Fig. 6 for temperatures between 320 K and 380 K, where they exhibit a visible α peak. These α peaks were fit to Eqs. (25) and (26). Initially, both τ_R and β_R were free fitting parameters. The resulting β_R values—which depend on the selected fitting range, varied between 0.77 and 0.80. We then fixed $\beta_R=0.78$ and repeated the fits. These fits are shown in the figure; the resulting τ_R values are shown in Fig. 5.

We carried out a free-volume fit [40] to the $\tau_R(T)$ values from the PCS and CD fits which is also shown in Fig. 5:

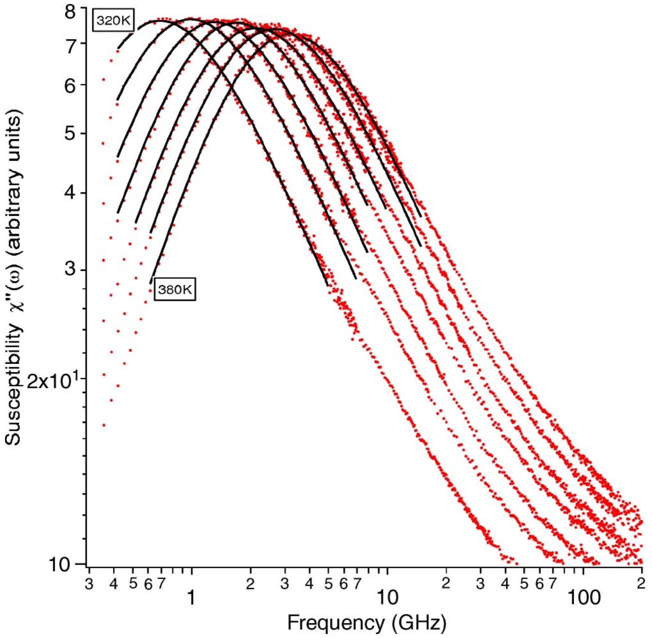

FIG. 6. (Color online) Fits of the α-peak region of the $\chi''(\omega)$ spectra for $T=320$, 330, 340, 350, 360, 370, and 380 K (left to right) to the Cole-Davidson function [Eq. (26)]. In these fits, β_R was fixed at 0.78. (The spectra have been slightly shifted vertically to improve visibility.)

$$\log_{10}(\tau_R) = A + B/\{T - T_0 + [(T-T_0)^2 + CT]^{1/2}\}, \tag{27}$$

which gave $A=-11.05$, $B=234.81$, $C=6.185$, and $T_0=248.44$ *K*. With this fit, we estimate $T_g \simeq 219.8$ *K*. The τ values obtained from this fit were used to fix the orientational $\tau_R(T)$ values for temperatures above the range of the PCS experiments and below 320 K where the α peak is not visible in the susceptibility spectra. Note that Eq. (27) includes four free fitting parameters and is therefore able to fit the data in Fig. 5 over a larger range of temperatures than the often-used VFT function which has three free parameters.

A number of previous experimental studies of salol have provided values for $\tau_\alpha(T)$. These include dielectric spectroscopy [41,42], PCS [43], optical Kerr effect (OKE) [44], and light scattering [6,35]. The $\tau_\alpha(T)$ values obtained from these measurements are all similar, but they show noticeable scatter. We note that recent molecular MCT calculations for diatomic molecules by Götze, Singh, Voigtmann, and Chong have shown that $\tau_\alpha^{(1)} > \tau_\alpha^{(2)} > \tau_\alpha^{(3)}$ where $\tau_\alpha^{(1)}$ applies to dielectric relaxation, $\tau_\alpha^{(2)}$ applies to VH light scattering, and $\tau_\alpha^{(3)}$ applies to the viscosity or the longitudinal modulus [45]. From our light scattering data and the dielectric data of Ref. [42], we find that, for $T=240$ K, $\langle\tau_\alpha^{(1)}\rangle = 0.18$ ms, $\langle\tau_\alpha^{(2)}\rangle = 0.15$ ms, and $\langle\tau_\alpha^{(3)}\rangle = 0.012$ ms, in agreement with their result.

We fit each $\tau_\alpha(T)$ set with the four-parameter extended free-volume model [Eq. (27)] and extrapolated to $\tau_\alpha=100$ s to estimate T_g. The resulting values ranged from 213 K to 219 K. The τ_α values found from the ϵ'' peaks in the dielectric data of Stickel, Fischer, and Richert [42] gave $T_g=217.8$ K.

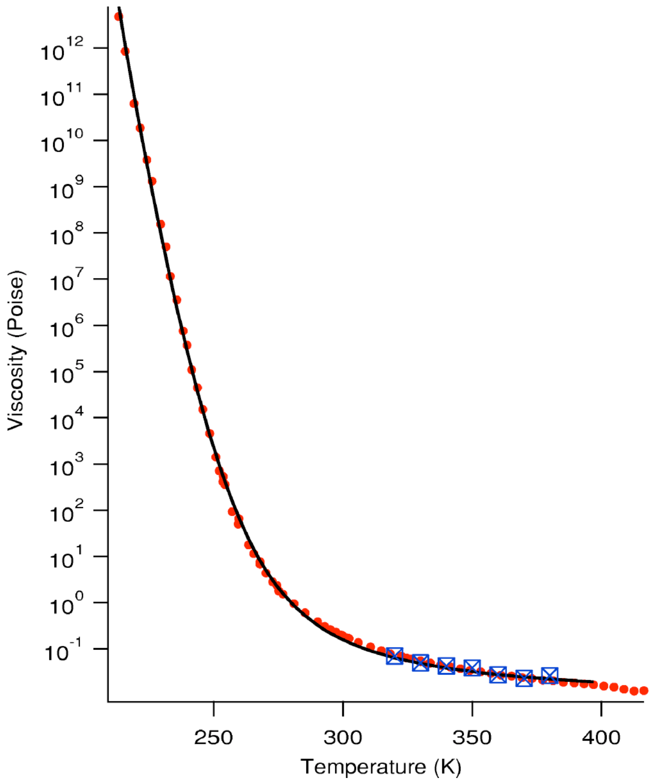

FIG. 7. (Color online) Salol viscosity data (points) from Refs. [46–48]. The solid line is a free-volume fit to Eq. (27) with $A=-2.157$, $B=123.0$, $C=3.984$, and $T_0=261.2$. The seven square symbols are viscosity values obtained from the I_{VH}^{90} high-temperature fits described in Sec. V A.

E. Viscosity

In our analysis of the VH 90° spectra, the static shear viscosity η_S will enter as a fitting parameter. The shear viscosity of salol was measured by Jantsch [46], Laughlin and Uhlmann [47], and Cukierman *et al.* [48] for temperatures between 416 K and 213 K. In this temperature range, the viscosity increases from 1.2×10^{-2} P to 4.8×10^{12} P. The combined viscosity data are plotted in Fig. 7 together with an extended free-volume fit to Eq. (27). The fit parameters obtained are $A=-2.157$, $B=123.0$, $C=3.984$, $T_0=261.2$ K. The resulting values, converted to Pa s, are given in Table III in Sec. V. Since the extrapolation of the fit to $\eta_S=10^{13}$ P gives $T_g\sim213$ K, we anticipate some uncertainty in the comparisons at low temperatures.

IV. DATA ANALYSIS 1: VH BACKSCATTERING SPECTRA

In the following two sections, we will analyze the 90° VH and VV spectra by fitting them to Eqs. (14) or (20) and (21), respectively. For both fits, the first term in each equation represents the pure rotational contribution which can be determined from the depolarized backscattering spectra. According to Eq. (20), these spectra should be described by Eq. (25).

In Sec. III D, we modeled $R(\omega)$ for the α-peak region with the Cole-Davidson function [Eq. (26)] from which the α-relaxation time τ_R was determined for temperatures from 380 K to 320 K. Since the 90° spectra will be analyzed in the frequency range $\sim0-15$ GHz, the fit for $R(\omega)$ for all temperatures must accurately represent the rotational spectrum in that frequency range. However, for frequencies above about five times that of the α peak, the Cole-Davidson approximation is inadequate.

As frequently discussed before, the α-relaxation region represents the final stage in the decay of the density or orientational correlation functions, which is preceded by, first, a very short-time (possibly oscillatory) "microscopic" region, and second, the fast-β-relaxation region. MCT leads to equations of motion for correlation functions $\phi_q(t)$ whose solutions exhibit these three dynamical regions [29]. Although we will not specifically follow the MCT approach here, we will utilize a simple phenomenological extension of the Cole-Davidson function which is consistent with predictions of MCT.

A. The hybrid model

Several recent publications have utilized a convenient semi-empirical model for memory functions $m(\omega)$ in supercooled liquids consisting of the Cole-Davidson function of Eq. (26) plus a power-law term ω^a which represents the fast relaxation process related to the t^{-a} critical decay of MCT (see, for example, Refs. [49–51]). In order to avoid having the ω^a term contribute at frequencies below the α peak, a cutoff term $e^{-t/\tau}$ can be included in the time domain memory function: $m_{crit}(t)=Bt^{-a}e^{-t/\tau}$. The resulting hybrid model memory function is then given by $R(\omega)=R_0H(\omega)$, where

$$H(\omega)=\{[1-(1+i\omega\tau)^{-\beta}]+i\omega p(\tau^{-1}+i\omega)^{a-1}\},\qquad(28)$$

where the Laplace transform convention of Eq. (13) has been used. [A different convention was used in Ref. [49] which gave a slightly different final form for $H(\omega)$.]

As an example, we have plotted $H(\omega)$ in Fig. 8 using the arbitrary parameters $\tau=100$ ns, $a=0.3$, $\beta=0.78$, $p=0.1$. The figure shows $\mathrm{Re}[H(\omega)]$ (upper frame) and $\mathrm{Im}[H(\omega)]$ (middle and lower frames). At low frequencies, $\mathrm{Re}[H(\omega)]$ is determined by H_{CD}, increasing from 0 and saturating at 1.0. Subsequently, the critical part H_{crit} increases as ω^a, so $\mathrm{Re}[H(\omega)]$ increases without limit as $\omega\to\infty$.

$\mathrm{Im}[H(\omega)]$, at low frequencies, is dominated by the α peak of the CD function. For frequencies above the α peak, $\mathrm{Im}[H_{crit}(\omega)]$ increases as ω^a, producing a minimum and, subsequently, a power-law increase. The high-frequency increase in both the real and imaginary parts of $H(\omega)$ is unphysical, but unimportant, since the fits will not extend to high frequencies.

Note that, in Eq. (25), the amplitude of $R(\omega)$ is fixed by the normalization condition:

$$\int_0^\infty \frac{1}{\omega}\mathrm{Im}\,R(\omega)d\omega=\pi/2.\qquad(29)$$

At high temperatures, R_0 can be determined by dividing the integrated spectrum of the CD fit [Eq. (26)] by the integrated experimental spectrum, which gave $R_0=0.9$. A similar value

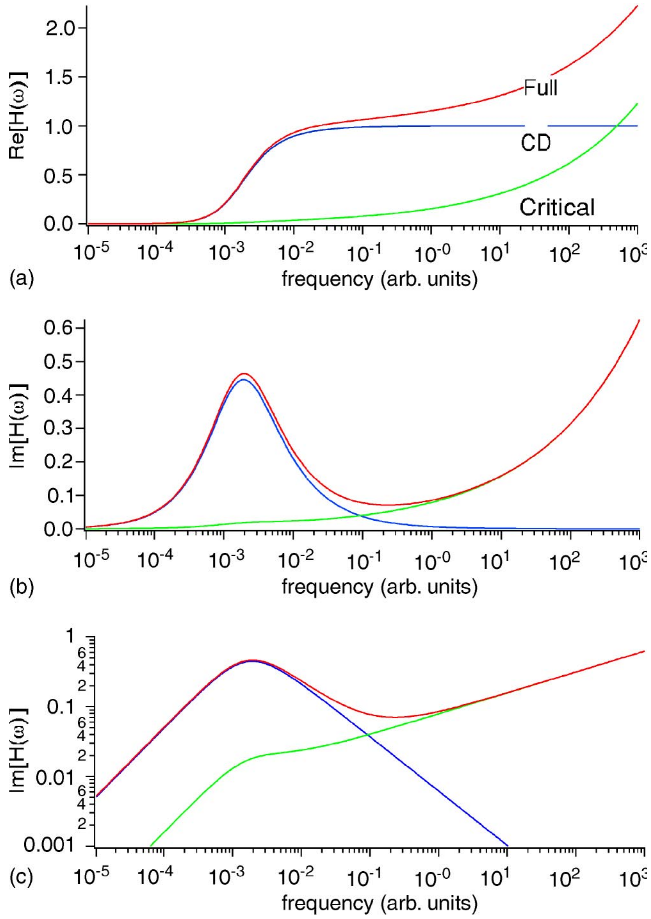

FIG. 8. (Color online) Real (a) and imaginary (b,c) parts of the Hybrid function $H(\omega)$ showing the full function and the CD and critical parts separately. The lower panel (c), plotted on a log scale, illustrates the effect of the cutoff factor that prevents the critical part from contributing significantly at frequencies below the α peak.

for R_0 was found from the KWW fits to the low-temperature PCS data [Eq. (24)]. The value of $R_0=0.9$ was therefore used in the analyses of the spectra for all temperatures. The procedure used to determine R_0 is described in the Appendix.

In analyzing the $I^{90}_{VH}(\vec{q},\omega)$ and $I^{90}_{VV}(\vec{q},\omega)$ spectra in the following sections, we will need several different memory functions. We will assume that they all have the form of Eq. (28) and that they all have the same value of a. We also assume that for every $H(\omega)$ the $\tau(T)$ values for $T>270$ K exhibit the same temperature dependence, although the absolute values may be different. For $T>T_C$, this assumption of α-scale universality is a prediction of MCT [29]. Below T_C, however, there is considerable evidence that translational and rotational time scales evolve differently [52]. We will return to this question briefly in Sec. VII.

B. Fits to $\chi''(\omega)$ spectra

The depolarized backscattering susceptibility spectra were fit to this hybrid model form:

$$\chi''(\omega) = A \times \mathrm{Im}\{[1-(1+i\omega\tau_R)^{-\beta_R}] + i\omega p_R(\tau_R^{-1}+i\omega)^{a-1}\}, \tag{30}$$

where p_R is the ratio of the critical contribution to the CD contribution, with the R_0 coefficient absorbed into the amplitude A. In the fits, $\tau_R(T)$ was fixed, as discussed in Sec. III, using the free-volume fit of Eq. (27) for all temperatures below 320 K where $\tau_R(T)$ had not been determined directly from the CD fits.

For the highest temperatures $(380-320\text{ K})$, the α peak dominates the spectrum and the critical exponent a is poorly defined. For these temperatures, we fixed $a=0.3$. For the intermediate temperatures $(310-250\text{ K})$, the full four-parameter Eq. (30) was used with the parameters A, p_R, a, and β_R all free.

For the lowest temperatures $(240-210\text{ K})$, only the fast-β relaxation and the extreme high-frequency wing of the α peak appear in the experimental spectral window, making the CD function poorly defined. In this region we used a simplified form for $\chi''(\omega)$ incorporating the high-frequency power-law region of the CD function and the critical decay:

$$\chi''(\omega) = A[\omega^{-\beta_R} + C\omega^{a}]. \tag{31}$$

The resulting values of C and a were used to compute p_R values for $T\leqslant 240$ K. However, the resulting values of p_R were very small. We attribute this to the presence, in the backscattering spectra at low temperatures, of spurious low-frequency intensity due to leakage of strong instrumental elastic scattering, visible in Fig. 9 for $T\leqslant 260$ K. We therefore used a linear fit to the p_R values for $T\geqslant 260$ K, extrapolated to lower temperatures, to obtain the values for $210\leqslant T\leqslant 255$ K shown in Table II.

Fortunately, the uncertainty in the low-temperature values of p_R and β_R do not affect the values found for a; the principal use of these low-temperature fits is the evaluation of a, the effective critical exponent which, as frequently found before, increases with decreasing temperature for $T<T_C$ ~ 255 K.

The fits are shown in Fig. 9 and the fitting parameters are listed in Table II. In the fitting procedure, a square-root weighting factor was chosen to optimize the low frequency region where the quality of the fit is most important for analyzing the 90° VH and VV spectra. In the analysis, $R(\omega)$ will be represented by Eq. (28) with the parameters taken from Table II.

An independent test of the $\chi''(\omega)$ spectra was made possible by the OKE study of salol by Hinze *et al.* [53]. $\chi''(\omega)$ spectra obtained by Fourier transformation of the OKE data for temperatures between 247 K and 340 K were provided by G. Hinze [54]. With small shifts in frequency, these OKE $\chi''(\omega)$ spectra were found to agree well with our optical spectra, except at the lowest temperatures where the minima of the OKE $\chi''(\omega)$ spectra are flatter than ours. We attribute this difference to the instrumental elastic scattering in our data at low frequencies and low temperatures mentioned above. We also found that the OKE $\chi''(\omega)$ spectra could be fit with the hybrid model [Eq. (30)] used to fit our spectra, with some minor differences in the resulting fitting parameters. We note,

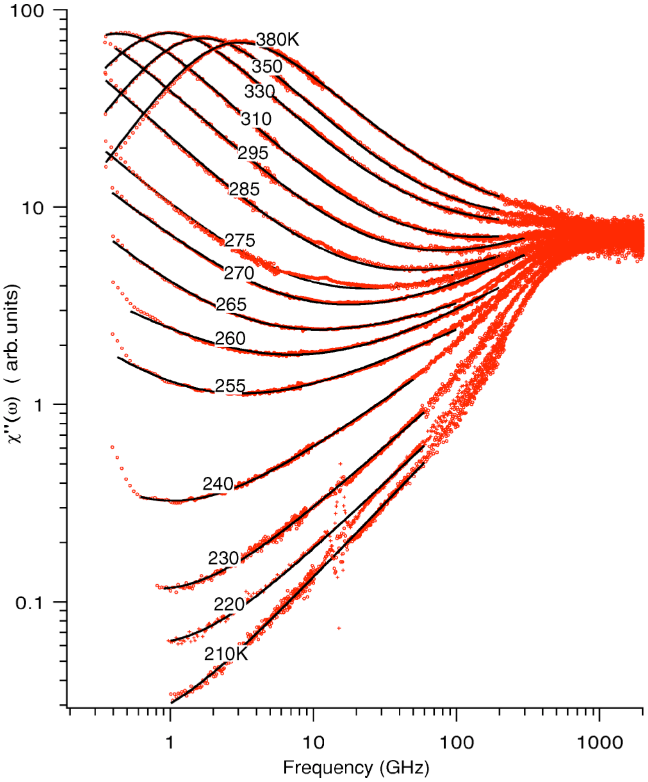

FIG. 9. (Color online) Fits of the depolarized backscattering susceptibility spectra $\chi''(\omega)$ to the hybrid model of Eq. (30) for 15 temperatures between 210 K and 380 K. Parameters obtained from the fits are listed in Table II.

however, that a very different analysis of the OKE data for five glass-forming materials (including salol) has been proposed recently by Cang, Novikov, and Fayer [55].

We also tried to fit the $\chi''(\omega)$ spectra using a "reduced version" of the hybrid model [Eq. (31)] in which the CD stretching coefficient β_R is set equal to the second MCT (Von Schweidler) exponent b. Since the exponents b and a are related by the MCT Γ-function relation [29], the number of fitting parameters is then decreased by one. This approach has been found to work quite well for toluene [50], picoline [51], and *n*-tricresyl phosphate [56]. However, for our salol data, the quality of the fits obtained with this additional constraint was significantly reduced in comparison with the fits obtained with both a and β_R free. (A similar result was found previously for propylene carbonate [49]).

C. Transport coefficients

In the following sections we will use viscoelastic generalizations of the four transport (friction) coefficients η_S, η_B, μ, and Γ. To minimize the number of additional parameters introduced, we will assume that $\eta_S(\omega)$ can be represented by the hybrid model of Eq. (28), and that $\eta_B(\omega) \propto \eta_S(\omega)$, but we will not constrain β_S for the viscosity to have the same value as β_R.

In analyzing the I_{VH}^{90} and I_{VV}^{90} spectra, the transport functions $\Gamma(\omega)$ and $\mu(\omega)$ will occur as the ratio $\Gamma(\omega)/\mu(\omega)$. We will assume that this ratio is independent of frequency (although it can depend on temperature), so the functional form of these two frequency-dependent transport coefficients will not influence the fits. We note that the assumption that $\mu(\omega)$ and $\Gamma(\omega)$ have the same frequency dependence has been made to avoid introducing additional parameters in the fitting procedure. There is, at present, no theoretical justification for this assumption.

V. DATA ANALYSIS 2: VH 90° SPECTRA

The theoretically predicted $I_{VH}^{90}(\vec{q},\omega)$ spectrum, with RT coupling included, is given by Eq. (14) or (20) with $r(\omega)$ and $P_T(\vec{q},\omega)$ given by Eqs. (16) and (17), and $D(\omega)$ given by Eq. (15). Setting $A^2b^2\langle|Q_{xy}|^2\rangle = I_0$, assuming that $\mu(\omega)$ and $\Gamma(\omega)$ have the same frequency dependence, and redefining the temperature-dependent translation-rotation coupling constant Λ by

$$\Lambda = \omega_R^2 \Lambda' z^2, \tag{32}$$

where

$$z = [\mu(\omega)/\Gamma(\omega)] \equiv z(T), \tag{33}$$

$R_1(\vec{q},\omega)$, the second term in $I_{VH}(\vec{q},\omega)$, becomes

$$R_1(\vec{q},\omega) = \frac{\Lambda(q^2/\rho_m)R^2(\omega)}{\omega^2 - (q^2/\rho_m)\omega\eta_T(\omega)} \tag{34}$$

with

$$\eta_T(\omega) = \eta_S(\omega) - \frac{\Lambda}{\omega} R^2(\omega)/[1 - R(\omega)], \tag{35}$$

where the final term gives the reduction in the viscosity due to RT coupling. Therefore, $I_{VH}^{90}(\vec{q},\omega)$ can be expressed as

$$I_{VH}^{90}(\vec{q},\omega) = \frac{I_0}{\omega}\mathrm{Im}\left[R(\omega) + \frac{(1/2)\Lambda(q^2/\rho_m)R^2(\omega)}{\omega^2 - (q^2/\rho_m)\{\omega\eta_S(\omega) - \Lambda R^2(\omega)/[1 - R(\omega)]\}}\right] \tag{36}$$

with $R(\omega)$ and $\omega\eta_S(\omega)$ given by

$$R(\omega) = R_0\{[1 - (1 + i\omega\tau_R)^{-\beta_R}] + i\omega p_R(\tau_R^{-1} + i\omega)^{a-1}\}, \tag{37}$$

$$\omega\eta_S(\omega) = \eta_S^{\circ}\{[1 - (1 + i\omega\tau_S)^{-\beta_S}] + i\omega p_S(\tau_S^{-1} + i\omega)^{a-1}\}. \tag{38}$$

Equation (36), with Λ defined by Eq. (32), is equivalent to the results in the recent publications of Dreyfus *et al.* [26,57]. It predicts that ω_B, the Brillouin peak frequency, will be at

$$\omega_B^2 = (q^2/\rho_m)[\omega\eta_S(\omega) - \Lambda R^2(\omega)]/[1 - R(\omega)]_{\omega=\omega_B} \tag{39}$$

or

TABLE II. Fit parameters obtained for the $\chi''(\omega)$ spectra using Eq. (30). τ_R values were fixed from PCS and α-peak data as described in the text

T (K)	A	$\tau_R(ns)$[a]	β_R	p_R=ratio[b]	a	range	χ^2[c]
380	1.43×10^{2}	6.152×10^{-2}	0.805	1.60×10^{-2}	0.30	0.3–100	8.19×10^{-6}
370	1.37×10^{2}	7.419×10^{-2}	0.800	1.40×10^{-2}	0.30	0.3–100	3.14×10^{-5}
360	1.56×10^{2}	9.139×10^{-2}	0.797	1.40×10^{-2}	0.30	0.3–100	2.50×10^{-5}
350	1.52×10^{2}	1.138×10^{-1}	0.800	1.40×10^{-2}	0.30	0.3–100	2.59×10^{-5}
340	1.53×10^{2}	1.466×10^{-1}	0.799	1.30×10^{-2}	0.30	0.3–100	6.70×10^{-5}
330	1.63×10^{2}	1.957×10^{-1}	0.789	1.20×10^{-2}	0.30	0.3–100	1.20×10^{-4}
320	1.64×10^{2}	2.864×10^{-1}	0.773	1.10×10^{-2}	0.30	0.3–100	4.80×10^{-5}
310	1.67×10^{2}	4.642×10^{-1}	0.743	9.10×10^{-3}	0.30	0.3–100	1.02×10^{-5}
300	1.90×10^{2}	8.460×10^{-1}	0.750	8.90×10^{-3}	0.30	0.3–100	1.20×10^{-4}
295	1.91×10^{2}	1.230	0.720	7.70×10^{-3}	0.30	0.3–300	2.10×10^{-7}
290	2.15×10^{2}	1.890	0.740	7.30×10^{-3}	0.30	0.3–300	2.10×10^{-4}
285	2.18×10^{2}	3.130	0.700	6.20×10^{-3}	0.30	0.3–300	6.20×10^{-4}
280	2.03×10^{2}	5.650	0.710	6.50×10^{-3}	0.30	0.3–300	7.60×10^{-5}
275	1.96×10^{2}	1.130×10^{1}	0.700	6.20×10^{-3}	0.30	0.3–300	9.50×10^{-5}
270	2.11×10^{2}	2.600×10^{1}	0.660	7.20×10^{-3}	0.28	0.4–150	2.80×10^{-5}
265	1.90×10^{2}	6.980×10^{1}	0.620	4.80×10^{-3}	0.31	0.4–150	2.40×10^{-5}
260	1.78×10^{2}	2.270×10^{2}	0.590	5.30×10^{-3}	0.30	0.5–70	7.20×10^{-6}
255	2.32×10^{2}	9.250×10^{2}	0.640	4.43×10^{-3}	0.32	0.3–45	5.60×10^{-6}
250	3.17×10^{2}	4.890×10^{3}	0.600	3.97×10^{-3}	0.40	0.6–50	3.64×10^{-9}
240	5.03×10^{1}	3.34×10^{5}	0.650	3.05×10^{-3}	0.52	0.8–50	1.52×10^{-8}
230	1.80×10^{1}	8.39×10^{7}	0.650	2.13×10^{-3}	0.65	0.9–50	1.84×10^{-7}
220	9.61×10^{2}	7.86×10^{10}	0.650	1.20×10^{-3}	0.69	1–60	3.90×10^{-5}
210	2.73×10^{2}	2.66×10^{14}	0.650	2.81×10^{-4}	0.76	1–60	5.00×10^{-7}

[a] τ values: 310–380 K from the α-peak CD fits; $T<310$ K from free volume fit.

[b] For $T\leqslant 255$ K the values shown were obtained by linear extrapolation of the values at higher T.

[c] All fits used $y^{1/2}$ as the weighting function except for 270–290 K which used $y^{-1/2}$ to emphasize the low-frequency region.

$$\omega_B = q\left[\frac{\omega\eta_S(\omega)}{\rho_m}\right]^{1/2}_{\omega=\omega_B}\left[1-\Lambda\frac{R^2(\omega)}{\omega\eta_S(\omega)}[1-R(\omega)]\right]^{1/2}_{\omega=\omega_B}. \tag{40}$$

The real part of the last factor in Eq. (40) is defined as the reduction factor r [23]. It gives the position of the Brillouin peak relative to what it would be if RT coupling were absent (so that $r=1$). For orthoterphenyl, Dreyfus *et al.* found $0.97\leqslant r\leqslant 0.995$; for $\mathrm{ZnCl_2}$, $r=0.95$, and for *m*-toluidine, $0.8\leqslant r\leqslant 0.93$. For salol, the analysis below gave values for the parameters at 275 K from which we find $r=0.75$, showing that RT coupling is more important in salol than in these other three materials. (We chose 275 K because it is in the region where the parameter values are most reliable.)

Note that, from Eqs. (35) and (40), the reduction of the shear viscosity due to RT coupling can be written as $\eta_T(\omega)=\eta_S(\omega)r^2(\omega)$. At 275 K, we found that $r^2(\omega)$ is essentially constant at 0.75, so that $\eta_T(\omega)\sim 0.5\,\eta_S(\omega)$.

The $I_{VH}^{90}(\vec{q},\omega)$ spectrum of Eq. (36) includes 12 parameters: q^2/ρ_m, a,τ_R, β_R, p_R, R_0, $\overset{\circ}{\eta}_S$, τ_S, β_S, p_s, Λ, and I_0. The first six have already been fixed from the analysis of depolarized backscattering spectra (Sec. IV) and from refractive index and density data (Sec. III). $\overset{\circ}{\eta}_S$ can be fixed via the relation $\beta_S\overset{\circ}{\eta}_S\tau_S=\eta_S$ [see Eq. (42)]. This leaves five unknown parameters: τ_S, β_S, p_s, Λ, and I_0. The 23 $I_{VH}^{90}(\omega)$ spectra, shown in Fig. 2, have qualitatively different forms in different temperature ranges that require different fitting strategies. We divided the 23 spectra into four temperature ranges and carried out the fits, starting from Eq. (36), as described below.

A. The high-temperature region

At high temperatures, the $I_{VH}^{90}(\vec{q},\omega)$ spectra exhibit the much-studied Rytov dip. In this temperature range the spectrum of Eq. (36) can be simplified. For low frequencies where the fast-β relaxation can be ignored and $\omega\tau\ll 1$, the frequency-dependent coefficients can be replaced by their $\omega\rightarrow 0$ limits:

$$R(\omega)=R^\circ\left[1-(1+i\omega\tau_R)^{-\beta_R}\right]\underset{\omega\tau\ll 1}{\rightarrow} iR^\circ\,\omega\beta_R\tau_R \tag{41}$$

and

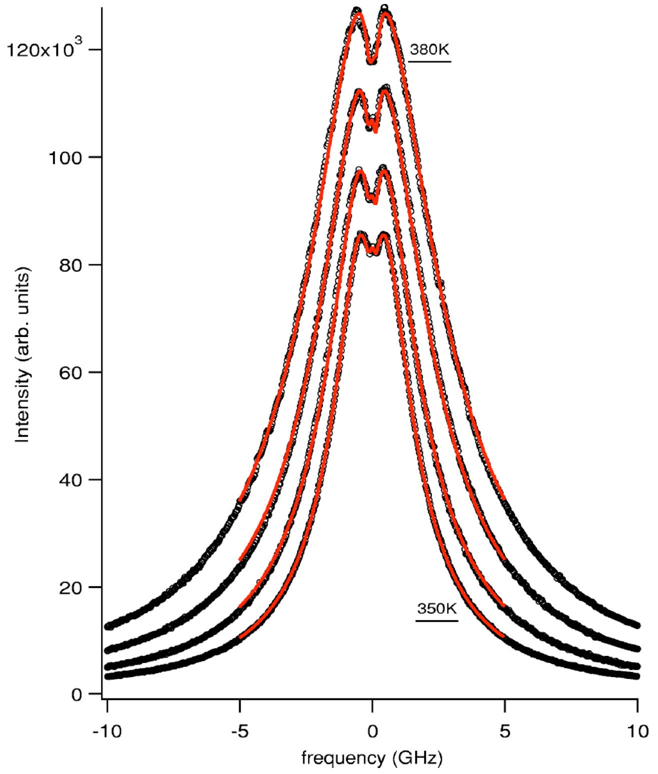

FIG. 10. (Color online) I_{VH}^{90} spectra at $T=380$, 370, 360, and 350 K with fits to Eq. (36). For these high-temperature fits, the frequency-dependence of $\eta_S(\omega)$ was ignored.

$$\omega\eta_S(\omega) = \eta_S^{\circ}[1-(1+i\omega\tau_S)^{-\beta_s}] \underset{\omega\tau\ll 1}{\longrightarrow} i\omega\beta_S\eta_S^{\circ}\tau_S = i\omega\eta_S. \tag{42}$$

In the low-frequency limit, with $\beta_R=1$, Eq. (36) is equivalent to the two-Lorentzian result of Andersen and Pecora [11,31] as shown in Ref. [21].

In fitting the $I_{VH}^{90}(\vec{q},\omega)$ spectra for $T=380$, 370, 360, and 350 K shown in Fig. 10, this simplification could be used for $\omega\eta_S(\omega)$ but not for $R(\omega)$ since at 350 K, for $\omega/2\pi \sim 6$ GHz, $\omega\tau_S \sim 0.25$ (see Sec. V D) but $\omega\tau_R \sim 4$. Therefore, the spectra were fit to Eq. (36), including convolution with the instrument function, with $\omega\eta_S(\omega)=i\omega\eta_S$ [Eq. (42)] and with the full $R(\omega)$ of Eq. (28) with $R_0=0.9$. In the fits, τ_R, β_R, a, and p_R were taken from the backscattering fit parameters in Table II, while I_0, Λ, and η_S were treated as free. We also added a δ-function with adjustable amplitude to the central channel where some weak elastic scattering was observed. The resulting parameters are given in Table III. The values found for η_S are also shown in Fig. 7 by square symbols and are seen to be in quite good agreement with experimental viscosity values.

For $T=340$, 330, and 320 K, the Rytov dip is no longer visible, and ignoring viscoelastic memory effects is no longer justified. However, it was still possible to extract values of η_S from the fits. These values are also included in Fig. 7. For temperatures between 320 K and 280 K this procedure was not possible. These spectra will be discussed below in Sec. V D.

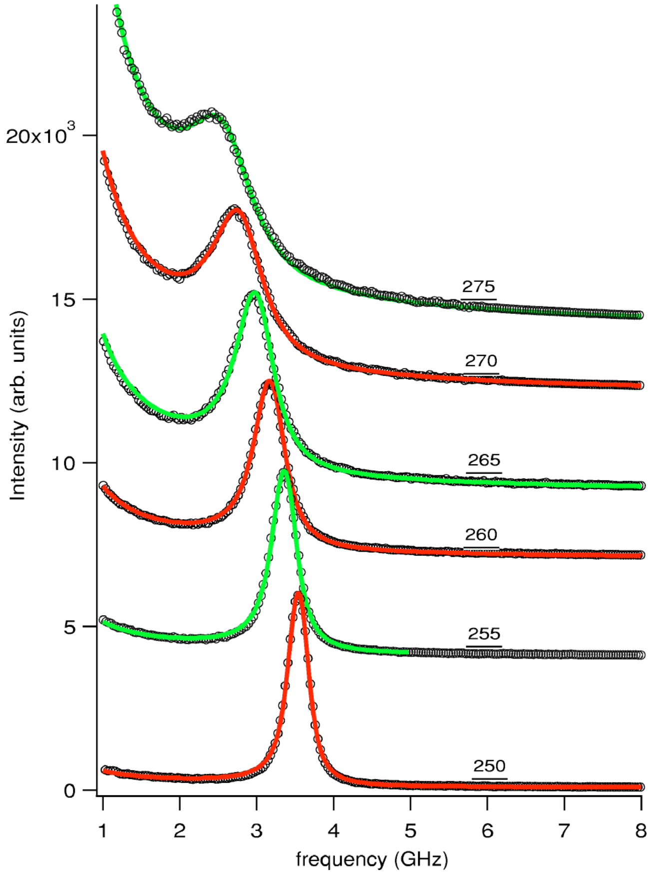

FIG. 11. (Color online) I_{VH}^{90} spectra with four-parameter fits at temperatures between 275 K and 250 K where the TA mode appears and sharpens into a well-defined acoustic mode.

B. The crossover region

Between ∼280 K and 250 K, a weak bump appears at ∼2 GHz and evolves into a fully developed transverse acoustic (TA) mode as shown in Fig. 11. In this temperature range, the spectra exhibit sufficient structure to fit them to the full $I_{VH}^{90}(\vec{q},\omega)$ equation [Eq. (36)].

In carrying out the fits, τ_R, β_R, p_R, and a were again taken from the I_{VH} backscattering fits (Table II) and R_0 was fixed at 0.9. The static shear viscosity η_S was taken from the free-volume fit to experimental viscosity data shown in Fig. 7 and listed in Table III. To further restrict the number of free fitting parameters, p_S in Eq. (38) was set equal to p_R. Also, the parameter η_S° was determined from Eq. (42) ($\beta_S\tau_S\eta_S^{\circ}=\eta_S$).

This left four free parameters: I_0, Λ, β_S, and τ_S. Fits were carried out using three different fitting ranges (1–5, 1–10, and 1–20 GHz) and two different weighting functions: $wt(i)=y_i^{-1/2}$ and $wt(i)=1$. The resulting fits for each T were nearly indistinguishable, although there was some scatter in the resulting fit parameters. Figure 11 shows one fit for each temperature from 275 K to 250 K. The values of the parameters I_0, Λ, β_S, and τ_S, averaged over the different fits, are given in part B of Table III. For $T\leqslant 250$ K, the fits showed strong anticorrelation between I_0 and Λ. For $T>275$ K where the spectrum is dominated by the orientational component, the fits obtained were less successful.

In the crossover region the RT coupling constant Λ was found to increase with decreasing temperature, an effect which is presumably due to the increasing density. We note that a similar temperature dependence for Λ was observed by Dreyfus *et al.* in $ZnCl_2$ [57] and metatoluidine [22]. In this region, we also found that β_S decreases rapidly with decreasing temperature, from $\beta_S = 0.49$ at 280 K to $\beta_S = 0.14$ at 250 K.

C. The low-temperature region

For temperatures below ~ 250 K, the $I_{VH}^{90}(\vec{q},\omega)$ spectra exhibit narrow transverse Brillouin components superimposed on a slowly varying background from the orientational $R(\omega)$ term. These spectra can be fit quite well by damped harmonic oscillator functions, and the fits show that at the lowest temperatures the observed linewidth is predominantly instrumental. Since so little information is contained in these low-temperature spectra, the number of free fitting parameters must be restricted.

We analyzed the spectra for 210, 220, 230, and 240 K using two approaches: (1) p_s free; for these fits, the parameters of $R(\omega)$ (including p_R) were fixed at the values found from the I_{VH} backscattering spectra given in Table II, with $R_0 = 0.9$. The value of I_0 was fixed by plotting the full $I(\vec{q},\omega)$ and the rotational part only with the data, and adjusting I_0 so that both theoretical curves coincide with the data in the frequency region above the Brillouin peak where $R_1(\vec{q},\omega) \ll R(\omega)$. β_s was arbitrarily fixed at 0.15. This left three free fitting parameters: Λ, τ_s, and p_s. The resulting fits are shown in Fig. 12. The corresponding fit parameters are shown in part *C*1 of Table III. In the table, fixed parameters are indicated by $*$. (2) p_s fixed: The second set of low-temperature fits was carried out with the constraint $p_s = p_R$. An additional "normal" damping γ_0 was introduced by adding a damping term $i\omega\gamma_0$ to $\omega\eta_S(\omega)$ in the denominator of Eq. (36). The values obtained using three free fitting parameters: Λ, τ_s, and γ_0 are shown in Table III in the last column of part *C*2. We note that the value found for Λ is very sensitive to the value chosen for I_0, as illustrated in the final two entries for $T = 210$ K so that all the resulting low-T parameter values for $T \leqslant 240$ K include considerable uncertainty.

D. The interpolation region

Finally, we return to the $I_{VH}^{90}(\vec{q},\omega)$ spectra for the temperature range 285 K $\leqslant T \leqslant$ 340 K which are shown in Fig. 13. At the highest temperatures in this range there is a slight residue of the Rytov dip at $\omega \sim 0$. At the lowest temperature a slight bulge in the wings signals the emergence of the TA mode at lower temperature. For these eight spectra, the high-temperature approximation used for $T \geqslant 350$ K in part A where viscoelasticity was ignored is no longer justified, while the spectra lack sufficient structure to permit use of the four-parameter fitting procedure used in part *B* for 250 K $\leqslant T \leqslant$ 280 K. We therefore arbitrarily fixed the remaining parameters, except for I_0, by interpolation. The RT coupling constant Λ has essentially the same value at $T = 350$ K (1.63) and 280 K (1.64); we therefore fixed $\Lambda = 1.63$ for this range.

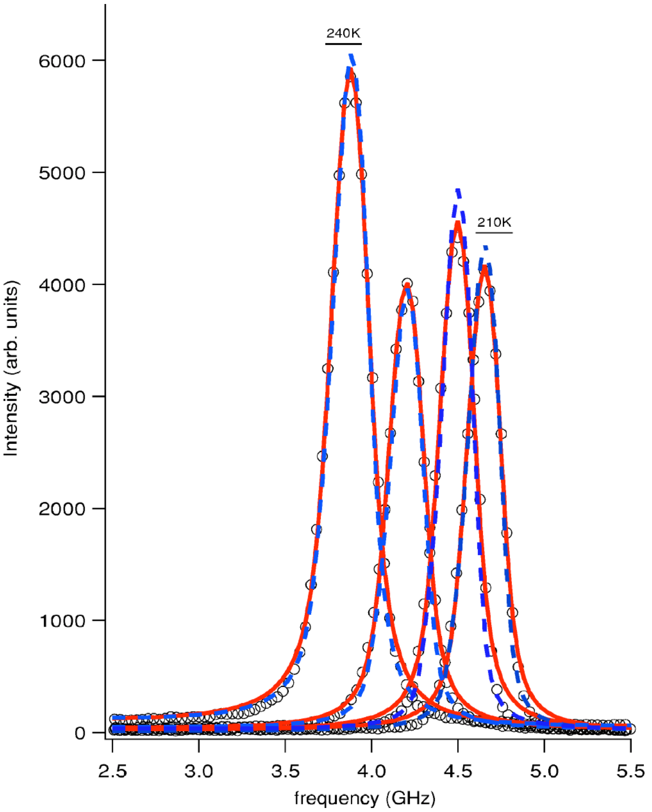

FIG. 12. (Color online) I_{VH}^{90} spectra at $T = 210$, 220, 230, and 240 K. Fits with Λ, τ_S, and p free (broken lines); fits with Λ, τ_S, and γ_0 free and $p_S = p_R$ (solid lines).

To obtain estimates of β_S and τ_S, we scaled their values for 250 K $\leqslant T \leqslant$ 280 K onto plots of β_R and τ_R found from the backscattering spectra, obtaining average values for the ratios β_S/β_R and τ_S/τ_R, and approximated β_S and τ_S at higher temperatures by continuing this scaling. The resulting values of the interpolated Λ, β_S, and τ_S, which were fixed in the fits, are given in part *D* of Table III. We then fit the spectra to Eq. (36) by varying I_0 only. The resulting fits are included in Fig. 13 as solid lines. The fits indicate that the parameters obtained by our interpolation process provide a reasonable description of the data.

For the VV 90° analysis in the following section, we used the same scaling procedure to estimate τ_S and β_S for high temperatures (350–380 K) as well.

VI. DATA ANALYSIS 3: VV 90° SPECTRA

The analysis of Pick *et al.* [26] and Franosch *et al.* [27] predicts that the 90° polarized $I_{VV}^{90}(\vec{q},\omega)$ spectra shown in Fig. 3 are described by Eq. (21). With the substitutions discussed in the preceding section, Eq. (21) for $I_{VV}(\vec{q},\omega)$ reduces to

$$I_{VV}(\vec{q},\omega) = \frac{A^2\langle|Q_{xy}|^2\rangle}{\omega} b^2 \mathrm{Im}\left\{\frac{4}{3}R(\omega) + \frac{q^2}{\rho_m}\Lambda'\omega_R^2 z^2\left[\frac{a\rho_m}{\Lambda' bz} + \frac{2}{3}R(\omega)\right]^2 P_L(\vec{q},\omega)\right\}. \quad (43)$$

Note that if the RT coupling vanishes, $\mu \to 0$ (so that $z \to 0$) and Eq. (43) reduces to

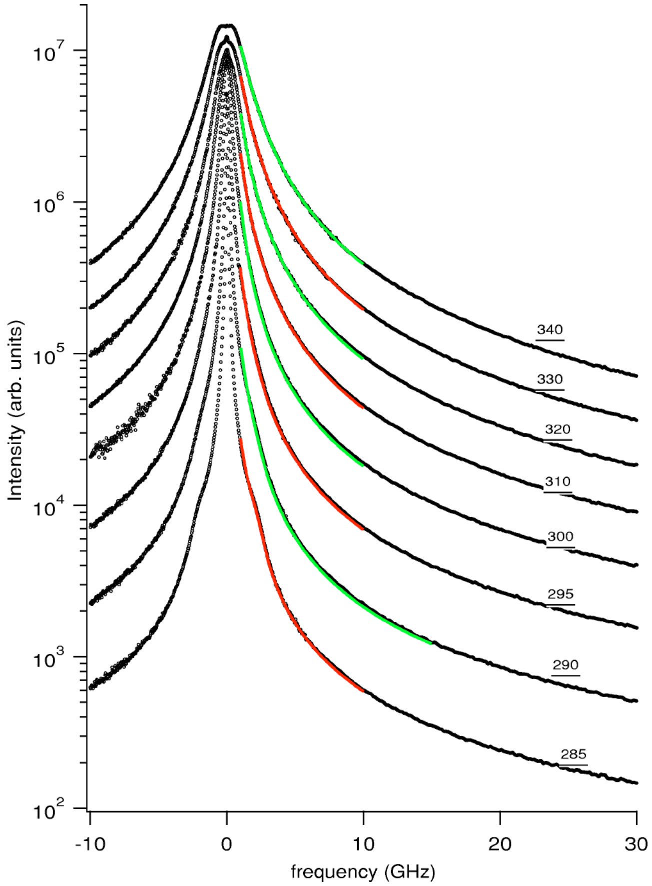

FIG. 13. (Color online) I_{VH}^{90} spectra in the temperature range 340–285 K. This interpolation region begins with the near disappearance of the Rytov dip and ends with the first signs of the incipient TA mode.

$$I_{VV}(\vec{q},\omega) = \frac{A^2\langle|Q_{xy}|^2\rangle}{\omega}\mathrm{Im}\left\{\frac{4}{3}b^2R(\omega) + \left[\frac{\rho_m}{\Lambda'}q^2\omega_R^2a^2\right]P_L(\vec{q},\omega)\right\}, \tag{44}$$

which is the conventional separation into rotational and translational components.

If we again define $A^2b^2\langle|Q_{xy}|^2\rangle = I_0$, represent the (unknown) parameter product $a\rho_m/\Lambda' bz$ by a single fitting parameter S, and use the definition of Λ of Eq. (32), $I_{VV}(\vec{q},\omega)$ becomes

$$I_{VV}(\vec{q},\omega) = \frac{I_0}{\omega}\mathrm{Im}\left\{\frac{4}{3}R(\omega) + \frac{q^2}{\rho_m}\Lambda\left[S + \frac{2}{3}R(\omega)\right]^2 P_L(\vec{q},\omega)\right\}. \tag{45}$$

Since $R(\omega)$ and Λ have already been determined, only I_0 and S are unknown, apart from the parameters occurring in the longitudinal propagator $P_L(\vec{q},\omega)$. From Eq. (22), $P_L(\vec{q},\omega)$ is given by

$$P_L(\vec{q},\omega) = \left\{\omega^2 - \frac{q^2}{\rho_m}[\rho_m C_0^2 + \omega\eta_L(\omega)]\right\}^{-1},$$

where the longitudinal viscosity $\eta_L(\omega)$ is given by Eq. (23). Setting $C_0 q = \omega_0$ and including a regular damping term γ_0 to represent damping processes other than coupling to structural relaxation, $P_L(\vec{q},\omega)$ can be written as

$$P_L(\vec{q},\omega) = \{\omega^2 - \omega_0^2 - (q^2/\rho_m)[\omega\eta_L(\omega) + i\omega\gamma_0]\}^{-1}. \tag{46}$$

From Eqs. (23) and (35), $\eta_L(\omega)$ can be expressed as

$$\eta_L(\omega) = \eta_B(\omega) + \frac{4}{3}\left[\eta_S(\omega) - \frac{\Lambda}{\omega}\frac{R^2(\omega)}{1-R(\omega)}\right]. \tag{47}$$

[Note that if RT coupling vanishes, the final reduction term in Eq. (47) will also vanish.]

The combination $\eta_B(\omega) + \frac{4}{3}\eta_S(\omega)$, without the final reduction factor in Eq. (47), is the conventional longitudinal viscosity $\eta_L'(\omega)$. It involves two different transport functions, the bulk and shear viscosities. To avoid introducing additional fitting parameters, we will assume that $\eta_B(\omega) \propto \eta_S(\omega)$ and write $\eta_B(\omega) + \frac{4}{3}\eta_S(\omega) = V\eta_S(\omega)$, where V is a fitting parameter. Therefore,

$$\eta_L(\omega) = \left[V\eta_S(\omega) - \frac{4}{3}\frac{\Lambda}{\omega}\frac{R^2(\omega)}{1-R(\omega)}\right]. \tag{48}$$

The assumption that $\eta_B(\omega) + \frac{4}{3}\eta_S(\omega) \propto \eta_S(\omega)$ is supported by the observation that the Brillouin linewidth maximum occurs near $T = 310$ K, where $\omega_B/2\pi \sim 7$ GHz. The linewidth maximum should occur when $\langle\tau_L\rangle$ (the mean relaxation time of the longitudinal viscosity) satisfies $\omega_B\langle\tau_L\rangle = 1$. For the Cole-Davidson function, $\langle\tau_L\rangle = \beta_{CD}\tau_{CD}$, so the maximum linewidth should occur at $\omega_B\beta\tau_L = 1$ or, approximately, at $\omega_B\tau_L \sim 1$. As shown in Table IV, $\omega_B\tau_S \sim 1$ near $T = 310$ K.

A. The difference spectra

In Eq. (45), the important frequency dependence of $I_{VV}(\vec{q},\omega)$ is in the second q-dependent term, so it is useful to eliminate the first $\frac{4}{3}R(\omega)$ term. To obtain the q-dependent part we scaled the VH backscattering spectrum at each temperature to match the high-frequency (30–50 GHz) region of $I_{VV}(\vec{q},\omega)$, as illustrated for 350 K in the upper panel of Fig. 14. In the lower panel we show the difference spectrum $I_{\mathrm{dif}}(\vec{q},\omega)$ obtained by subtracting the scaled $I_{VH}^{back}(\omega)$ spectrum from the $I_{VV}^{90}(\vec{q},\omega)$ spectrum. Note that this difference spectrum is zero at high frequencies as expected, but *negative* at low frequencies. The plot has been constructed with a logarithmic frequency axis to enhance the visibility of this negative region. The inset to the upper panel also shows that, at low frequencies, $I_{VV}^{90}(\vec{q},\omega)$ falls slightly below the scaled $I_{VH}^{back}(\omega)$ spectrum, producing the negative "VV dip" region in the difference spectrum.

In order to be sure that the $I_{VV}^{back}(\omega)$ spectra did not contain extra low-frequency signal due to leakage of elastic scattering, we compared them to spectra obtained with an empty cell. At the lowest temperatures, there was some spurious signal as mentioned in Sec. IV B. However, for $T \geqslant 250$ K, no leakage signal was found.

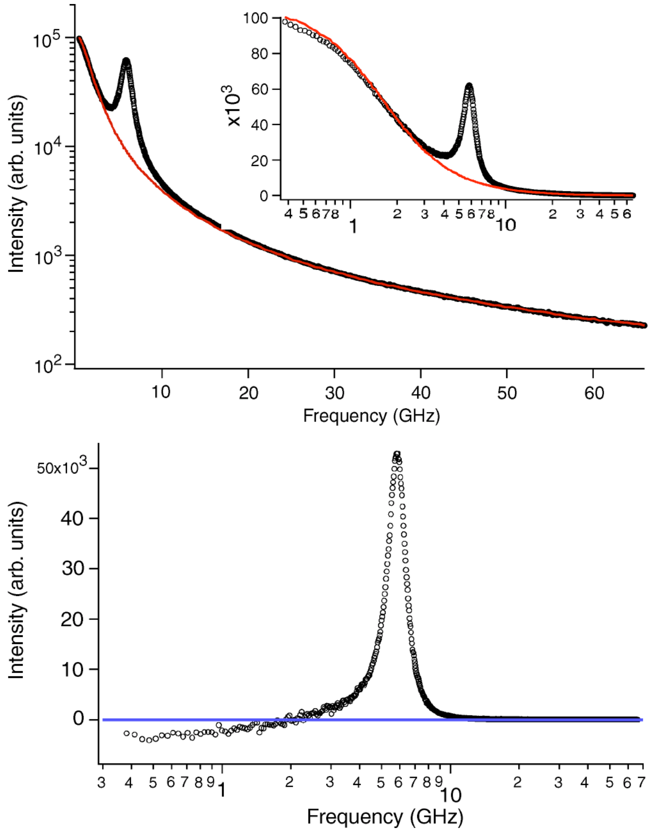

FIG. 14. (Color online) Generating the $I_{\mathrm{dif}}(\omega)$ difference spectra. Upper panel: I_{VV}^{90} spectrum (points) and scaled I_{VH}-back spectrum (line) for $T=350$ K. Inset: same, with linear y and log x scales. Lower panel: the difference spectrum obtained by subtracting the scaled I_{VH}-back spectrum from the I_{VV}^{90} spectrum. (The line is $I=0$.)

Fits were carried out both with and without RT coupling in order to evaluate the changes this coupling causes.

B. Fits to the full theory

We first fit the $I_{\mathrm{dif}}(\vec{q},\omega)$ spectra using the full theory. The parameters in the orientational function $R(\omega)$ were again taken from the VH backscattering fits, and Λ from the I_{VH}^{90} fits. To further reduce the number of free fitting parameters, we began by evaluating I_0 and γ_0 separately.

I_0: In the high-frequency region of $I_{VV}^{90}(\vec{q},\omega)$, $P_L(\vec{q},\omega)$ decreases as ω^{-2}, so that the second term in Eq. (45) is negligible with respect to the first term. Therefore,

$$I_{VV}(\vec{q},\omega)_{(\omega \gg \omega_B)} = \frac{I_0}{\omega}\mathrm{Im}\left[\frac{4}{3}R(\omega)\right]. \tag{49}$$

To fix I_0, we fit $I_{VV}^{90}(\vec{q},\omega)$ at frequencies between 40 and 60 GHz, where the spectra should be purely orientational, to Eq. (49), using the parameters for $R(\omega)$ given in Table II. The values of I_0 (the single free fitting parameter) obtained from the fits are given in Table IV.

γ_0: To fix the value of γ_0, we first fit the $I_{VV}^{90}(\vec{q},\omega)$ spectra in the region of the Brillouin peak to a damped harmonic oscillator function added to the orientational term:

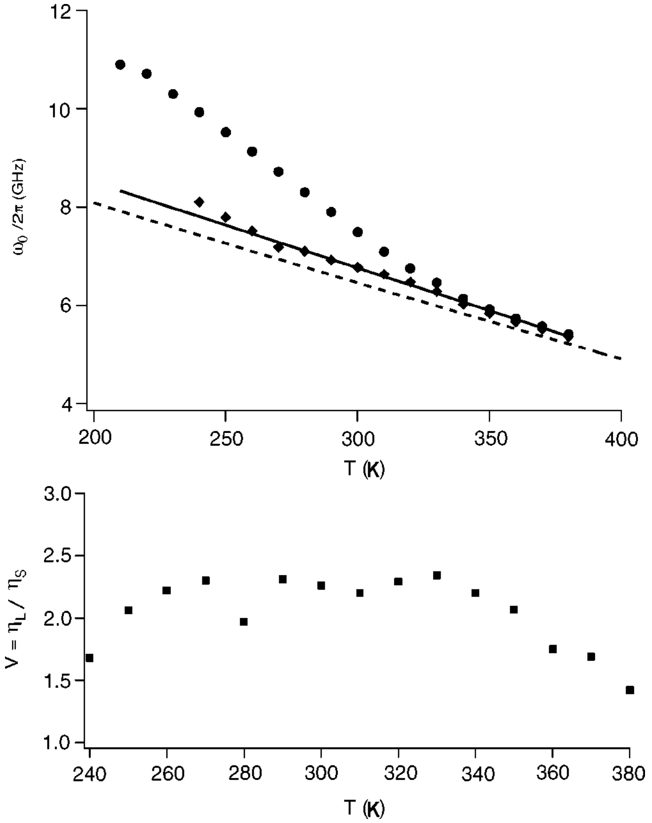

FIG. 15. (Color online) Upper panel: ω_B values from damped oscillator fits to Brillouin peaks (solid circles), ω_0 from ultrasonic data (broken line), and with arbitrary 3% increase to match ω_B at high temperatures (solid line). Diamonds indicate ω_0 values obtained from the full fits, with Γ_0 fixed at $T/600$. Lower panel: $V=\eta_L/\eta_S$ from the full fits indicating a near constant ratio of ~2.3.

$$I_{VV}(\vec{q},\omega) = \frac{I_0}{\omega}\mathrm{Im}\left\{\frac{4}{3}R(\omega) + B(\omega^2-\omega_B^2-i\omega\Gamma_B)^{-1}\right\} \tag{50}$$

with B, ω_B, and Γ_B as free parameters. The values obtained for $\omega_B/2\pi$ and $\Gamma_B/2\pi$ (in GHz) are given in Table IV and ω_B is also plotted in the upper panel of Fig. 15. In the figure, we also plot $\omega_0=C_0q$, using $C(T)$ obtained from a linear fit to high-temperature 10 MHz ultrasonic data for salol provided by B. Bonello [58]. This result, shown by the broken line in the figure, falls below the high-temperature ω_B values by about 3%, which lies within experimental error. Since ω_B and ω_0 should agree at high temperatures, we increased the C_0q values by 3%, producing the solid line in the figure which corresponds to $\omega_0/2\pi=11.988-0.0174\times T$ (GHz).

In carrying out the fits, as discussed below, we tried various fixed values for $\gamma_0(T)$ and chose the one for which the resulting values of ω_0 fell closest to this line. This led us to fix $\Gamma_0=(q^2/\rho_m)\gamma_0=T/600$ (GHz). With I_0 and γ_0 fixed, the full set of difference spectra $I_{\mathrm{dif}}=I_{VV}^{90}-\text{scaled } I_{VH}^{back}$, obtained with the procedure illustrated in Fig. 14, were fit to Eq. (45) with the $\frac{4}{3}R(\omega)$ term removed:

$$I_{dif}(\vec{q},\omega) = \frac{I_0}{\omega}\mathrm{Im}\left\{\frac{q^2}{\rho_m}\Lambda\left[S+\frac{2}{3}R(\omega)\right]^2 P_L(\vec{q},\omega)\right\} \tag{51}$$

with $P_L(\vec{q},\omega)$ given by Eqs. (46) and (47):

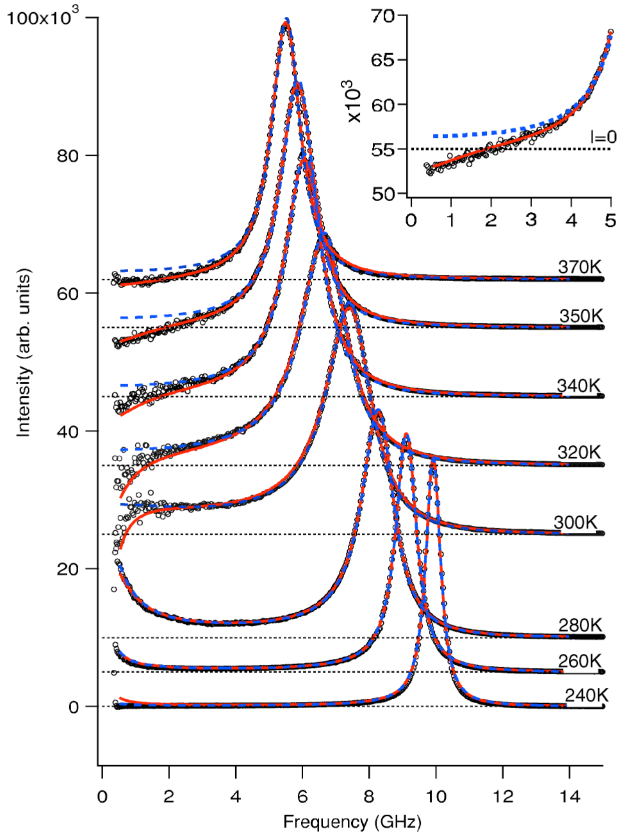

FIG. 16. (Color online) Difference spectra for $T=240$, 260, 280, 300, 320, 340, 350, and 370 K. The spectra have been scaled and shifted vertically for visibility. Solid lines: fits to the full theory; broken lines: fits to the density-fluctuation-only model. The dotted lines indicate the $I=0$ baseline for each spectrum. Inset: Low-frequency region for $T=350$ K.

$$P_L(\vec{q},\omega) = \left\{ \omega^2 - \omega_0^2 - i\omega\Gamma_0 - \frac{q^2}{\rho_m}\left[V\omega\eta_S(\omega) - \frac{4}{3}\Lambda\frac{R^2(\omega)}{1-R(\omega)} \right]^{-1} \right\}. \tag{52}$$

In the fits, ω_0, V, and S were the free fitting parameters.

The fit results for $T=240-370$ K are shown in Fig. 16 by the solid lines. The values of ω_0 obtained in the fits are shown in Fig. 15 and show the consistency of our choice for $\Gamma_0(T)$. Furthermore, with this choice, $\Gamma_0(T)$ agrees closely at low temperatures with Γ_B found from the damped oscillator fits.

There is an abrupt change in the low-frequency structure of $I_{VV}(\vec{q},\omega)$ between 280 K and 300 K where the VV dip first appears. For temperatures above 280 K, an extrapolation procedure was used to estimate τ_S and β_S, as described in Sec. V D. To be sure that the theoretical spectra were not affected by the changes in these parameters, we reanalyzed the 300 K spectrum constraining τ_S/τ_R and β_S/β_R to have the same values at 300 K as at 280 K. The resulting 300 K fit spectrum was slightly different in the region of the Brillouin peak, but was indistinguishable from the original fit in the vicinity of the VV dip. This shows that the VV dip feature is not sensitive to the detailed form of $\eta_S(\omega)$.

The viscosity ratio $V=\eta_L/\eta_S$ computed from the full fits is included in Table IV, and is also shown in the lower panel of Fig. 15. In the temperature range $260\ \mathrm{K} \leqslant T \leqslant 340$ K, $\eta_L/\eta_S \sim 2.3$, indicating that in this region η_S and η_B are essentially equal, although η_S changes by seven orders of magnitude in this range.

C. Fits without rotation-translation coupling

If RT coupling is ignored (as has been done in previous analyses of VV-polarized Brillouin spectra), then $I_{dif}(\vec{q},\omega)$ is given by Eq. (44) with the $R(\omega)$ term removed. Also, in Eq. (52) for $P_L(\vec{q},\omega)$, the final term in the brackets, which gives the reduction of the shear viscosity due to RT coupling, vanishes. Therefore, we have

$$I_{dif}(\vec{q},\omega) = \frac{A}{\omega}\mathrm{Im}[P_L(\vec{q},\omega)], \tag{53}$$

where $A=I_0(\rho_m/\Lambda')q^2a^2\omega_R^2$ and

$$P_L(\vec{q},\omega) = [\omega^2 - \omega_0^2 - i\omega\Gamma_0 - \Delta^2 H_S(\omega)]^{-1}. \tag{54}$$

$H_S(\omega)$ is the hybrid function for $\omega\eta_S(\omega)=\mathring{\eta}_S H_S(\omega)$ in Eq. (38) and $\Delta^2=(q^2/\rho_m)V\mathring{\eta}_S$.

We fit the difference spectra to Eqs. (53) and (54), with the parameters appearing in $H_S(\omega)$ fixed from the I_{VH}^{90} fits, listed in Table III. This is a conventional analysis of Brillouin scattering spectra, similar to that carried out previously for many other materials (e.g., Refs. [49–51]). In the fits, ω_o, Δ^2, and A were the free parameters (which is equivalent to varying ω_o, V, and S in the full fits).

We tried using various fixed values for Γ_0 as in the full fits, and found that fixing $\Gamma_0=T/600$ again produced values of ω_0 quite close to the straight line in Fig. 15. These "density-fluctuation-only" fits are shown in Fig. 16 by broken lines. The fits are all excellent for frequencies above 2 GHz, but for temperatures above 280 K the low-frequency regions of the fits become increasingly less satisfactory because the spectra become negative while the theoretical fits to Eqs. (53) and (54) are always positive—as they must be [27]. [Note that while the difference spectra have low-frequency negative regions, the full $I_{VV}(\vec{q},\omega)$ spectra are everywhere positive at all temperatures.]

From the results of these fits, we also computed the temperature dependence of the viscosity ratio $V=\eta_L/\eta_S$. Since $\eta_S=\beta_S\mathring{\eta}_S\tau_S$ and $\eta_L=V\eta_S$ while $\Delta^2=(q^2/\rho_m)V\mathring{\eta}_S$, the static longitudinal viscosity η_L is therefore given by

$$\eta_L = \beta_S\tau_S\Delta^2/(q^2/\rho_m). \tag{55}$$

We found that $\eta_L/\eta_S \sim 2$, independent of temperature, in the temperature range 240 K–380 K, similar to—but slightly smaller than—the result obtained with the full fits, presumably due to the neglect of the reduction factor.

D. Comparison of fits with and without rotation-translation coupling

Figure 16 shows both the full fits (solid lines), and the density-fluctuation-only fits (broken lines). At higher temperatures, the low-frequency region is fit much better with the full theory than with the density-fluctuation-only theory, showing that RT coupling, which is ignored in the conventional density-fluctuation-only analysis, is the source of the negative region. For temperatures below 290 K, the effects of RT coupling are limited to frequencies too low to be visible within the spectral window accessible to our experiments, so that the two fits are indistinguishable.

Referring to Fig. 4 in Ref. [26], there is the same tendency for the full theory to fall below the density-fluctuation-only fits to it at low frequencies when $\omega_B\tau \simeq 1$. Also, their Figs. 1 and 2 illustrate the temperature evolution of the intensity due to both the orientation-only channel $[R^2(\omega)]$ and the cross term $[SR(\omega)]$ in Eq. (51). In particular, their Fig. 2 also shows that the negative contribution moves to lower frequencies as T decreases and τ increases. Nevertheless, there are differences between the line shapes in their figure and ours which are due to the use of a single relaxation time in their calculations, while for salol, as shown in Table IV, the condition $\omega_B\tau \simeq 1$ occurs near 310 K for τ_S, while for τ_R it has not yet been reached at 380 K, the highest temperature that we studied.

E. Origin of the VV dip

The VV dip phenomenon is a consequence of RT coupling. The uniaxial strain that characterizes a longitudinal acoustic mode is a superposition of simple compression and shear strain. In liquids composed of anisotropic molecules, the time-dependent longitudinal strain induces time-dependent molecular orientation, creating a second light scattering mechanism. Physically, the uniaxial strain induces a preferential orientation of the long axes of the molecules in the plane perpendicular to $\vec{q}$, adding to $\delta\epsilon_{yy}$ which determines the VV scattered intensity [Eq. (10a)].

Referring to the equation of motion for $\bar{\bar{Q}}$ [Eq. (2)], the steady-state solution gives Q_{ij} proportional to the strain rate τ_{ij}. Therefore, for oscillatory LA waves in the low-frequency limit (where $\omega\tau \ll 1$), if $\delta\rho$ is real, then Q_{ij} is imaginary. Mathematically, this is reflected in the optical coupling function $C(\omega)=[S+(2/3)R(\omega)]^2$ in Eq. (51) which, in this limit, becomes

$$\left[S+\tfrac{2}{3}R(\omega)\right]^2 \rightarrow \left[S+i\omega\tfrac{2}{3}R_0\beta_R\tau_R\right]^2 \rightarrow \left[S^2+i\omega\tfrac{4}{3}R_0\beta_R\tau_R S\right] \tag{56}$$

and, from Eqs. (51) and (52) in this limit,

$$\begin{aligned} I_{dif}(\vec{q},\omega) \underset{\omega\tau \ll 1}{\rightarrow} & \frac{I_0 q^2 \Lambda}{\rho_m \omega_0^4}\left[S^2 \eta_L \frac{q^2}{\rho_m} - S\omega_0^2 \frac{4}{3} R_0 \beta_R \tau_R\right] \\ & = \frac{I_0 q^4 \Lambda \eta_L S}{\rho_m \omega_0^4}\left[\frac{S}{\rho_m} - \frac{4}{3}\left(\frac{\omega_0}{q}\right)^2 R_0 \beta_R \frac{\tau_R}{\eta_L}\right]. \end{aligned} \tag{57}$$

The second term in the square brackets, being negative, reduces the intensity at low frequencies; if its magnitude exceeds that of the first (positive) term, then the low-frequency intensity will be negative. But this is no longer true at frequencies $\omega > \tau_R^{-1}$ where Q_{ij} can no longer follow the oscillating strain. Since τ_R increases with decreasing temperature, the width of the VV dip will decrease.

With decreasing temperature, η_L also increases, causing the prefactor of the square-bracket term in Eq. (57) to increase. The VV dip thus becomes both deeper and narrower with decreasing T; it disappears from the experimental spectra when its width becomes smaller than the lower limit of the experimental frequency window.

F. Relation between the Mountain mode and the VV dip

There are two important temperature-dependent features that appear in the $I_{VV}^{90}(\vec{q},\omega)$ spectra, the Mountain mode and the VV dip, both of which become much more visible after subtraction of the pure orientational contribution to give $I_{dif}(\vec{q},\omega)$ (see Fig 16).

At 240 K, the LA Brillouin component is very narrow (its width is mostly instrumental) and it lies above a flat $I \sim 0$ baseline. At this low temperature, $\omega_B\tau \gg 1$ for all relaxation processes. As T increases, $\omega_B\tau_L$ decreases, where τ_L (which we assume to be equal to τ_S), is the structural relaxation time appropriate for longitudinal acoustic waves. The Brillouin linewidth increases, reaching a maximum near 310 K where $\omega_B\tau_L \sim 1$. The much-studied "Mountain mode," produced by the coupling of the sound wave to structural relaxation, first appears at the low-frequency edge of the spectrum near $T=260$ K and broadens with increasing T. By $T=300$ K it has become a nearly flat contribution on the low-frequency side of the Brillouin peak. With further increase of T, its amplitude decreases.

At 300 K, the "VV-dip" begins to appear within our spectral window, causing the difference spectrum to become negative at the lowest frequencies. By 350 K, the negative VV-dip region extends up to about 2 GHz, and is very visible because the Mountain mode intensity is very weak.

Note that the Mountain mode appears at lower temperatures than the VV-dip because τ_R is about 15 times larger than τ_L for salol, as shown in Table IV. The large difference between the two relaxation times results in a convenient temperature separation of the two effects.

The characteristics of the VV-dip phenomenon observed in this experiment agree fully with the predicted effects of RT coupling as described in the analysis of Refs. [26,27]. The reason that it has not been observed previously is suggested by the upper panel of Fig. 14. The full $I_{VV}^{90}(\vec{q},\omega)$ spectrum can be fit quite well by the superposition of the rotational spectrum and the LA spectrum. It is only when the *difference* spectrum is examined that the small low-frequency VV dip becomes apparent.

VII. DISCUSSION AND CONCLUSIONS

We have carried out an analysis of three sets of light-scattering spectra of the molecular glassforming liquid salol: $I_{VH}^{back}(\omega)$, $I_{VH}^{90}(\vec{q},\omega)$, and $I_{VV}^{90}(\vec{q},\omega)$. The analysis, which was designed to explore the consequences of rotation-translation coupling, was based on the phenomenological theory of Refs. [21,26] and the parallel Zwanzig-Mori analysis of Ref. [27]. The $I_{VH}^{back}(\omega)$ spectra, which display the pure orientational dynamics represented by $R(\omega)$, were fit to a "hybrid function" that combines the Cole-Davidson α-relaxation function with an ω^a power law to model the fast-β-relaxation region.

With all the parameters of the orientational function $R(\omega)$ fixed from these backscattering fits, we next analyzed the $I_{VH}^{90}(\vec{q},\omega)$ spectra to obtain the parameters of the shear viscosity function $\eta_S(\omega)$, and the RT coupling constant Λ. Finally, with these parameters and those of $R(\omega)$ fixed, we analyzed the $I_{VH}^{90}(\vec{q},\omega)$ spectra. In this third experiment, we observed—for the first time—a feature predicted by the theory which we have called the VV dip.

The fits gave generally excellent agreement with predictions of the theory. Nevertheless, there are several approximations built into the procedure that should be further studied. (1) The orientational dynamics are based on the assumption of axisymmetric molecules [34]. (2) Temperature fluctuations are not included. (3) $R(\omega)$, and the four transport coefficients $\Gamma(\omega)$, $\mu(\omega)$, $\eta_S(\omega)$, and $\eta_B(\omega)$ are all assumed to have the same functional form. (4) The ratio $\Gamma(\omega)/\mu(\omega)$ is assumed to be independent of ω although it can depend on T; the same assumption was made for $\eta_B(\omega)/\eta_S(\omega)$. What effect these assumptions have cannot presently be evaluated, although it seems unlikely that the fits would be significantly improved by relaxing them. It would be interesting to compare some of our results with different experiments, e.g., dynamic viscosity measurements.

Recently, time-resolved optical Kerr effect data have been analyzed for benzophenone and salol by Götze and Sperl, and for benzene by Ricci *et al.* [59]. Both groups utilized a two-correlator schematic MCT approach (the Sjögren model) in which a coupling constant V_A plays the role of our RT coupling constant Λ. For all three materials V_A was found to increase with decreasing T, qualitatively similar to the behavior of Λ indicated in Table III. Presumably, this increase is caused by the increase in density due to thermal contraction.

There is another interesting question related to glass-transition dynamics that we can use our results to discuss, often called the separation of time scales. In its most familiar form, it concerns the different temperature dependences of the translational and rotational diffusion constants D_T and D_R. At high temperatures, both constants follow $1/\eta_S$, but at lower temperatures, D_T is enhanced [52,60]. There is a second, weaker separation effect, concerning D_R and η_S. Chang and Sillescu [60] examined the ratio $\eta_S/T\tau_{\mathrm{diel}}$ (where τ_{diel} is the mean dielectric relaxation time) for a variety of glass-forming liquids and found that, while essentially constant at high temperatures, this ratio increases by approximately one order of magnitude on approaching T_g. If one assumes that the dielectric relaxation time τ_{diel} is proportional to $\langle\tau_R\rangle$, then a similar increase should occur in $\eta_S/T\langle\tau_R\rangle$.

We therefore examined the ratio $\eta_S/T\beta_R\tau_R$, using the values for τ_R and β_R in Table II and for η_S in Table III. We found that the value of this ratio was approximately constant for temperatures above 250 K, and increased with decreasing temperature between 250 K and 220 K by approximately a factor of 4.

A. Comparison with previous experiments

The temperature evolution of the $I_{VH}^{90}(\vec{q},\omega)$ salol spectrum was first studied by Fabelinskii *et al.* using photographic detection [2]. They found that the "doublet separation" (the Rytov dip) can be followed down to 320 K where it disappears, reappearing again (as TA modes) at ~275 K. Enright and Stoicheff [7] used photoelectric detection and analyzed their spectra with the two-variable Anderson-Pecora theory [11]. They found that the Rytov dip disappears on cooling at 335 K, while the TA modes first appear at 275 K, which is very close to our results. Wang and Zhang [17] and Vaucamps *et al.* [36] obtained results for the $I_{VH}^{90}(\vec{q},\omega)$ spectrum consistent with those of Enright and Stoicheff. The difference between these results and those of Fabelinskii *et al.* is presumably due to differences in instrumental resolution.

Sidebottom and Sorenson [43] performed PCS experiments on salol using small angle scattering (1.1° and 2.3°). For temperatures between 239 K and 218 K they observed a mode—which they designated as "the Mountain mode"—that they fit to the KWW function of Eq. (24). The values of τ and β that they found are in reasonably good agreement with our τ_R and β_R values with an apparent T offset of about 3 K. We believe that what they observed was the orientational spectrum [Eq. (25)] which is much more intense than the Mountain mode. The fact that they found values for τ_R and β_R at these small angles similar to those we found in backscattering shows that $R(\omega)$ is q independent as we have assumed.

The temperature evolution of the polarized Brillouin scattering spectrum of salol has been studied by Wang and Zhang [17] and by Dreyfus *et al.* [37]. Both experiments found temperature-dependent frequencies and linewidths similar to those reported here. Both, however, analyzed the data assuming that the translational and orientational dynamics produce independent spectra which can therefore be analyzed as a simple superposition. While this procedure gives good fits to the data, the VV-dip phenomenon reported here shows that it is not strictly correct.

Salol has also been studied by time-resolved spectroscopy techniques. Yang and Nelson [61] performed an unpolarized transient grating (TG) experiment between 270 K and 240 K and analyzed it ignoring the molecular anisotropy. They deduced from this analysis the longitudinal relaxation time τ_α and the corresponding stretching coefficient. Their relaxation time values are in good agreement with our τ_s values, but their stretching parameters are, at each temperature, substantially higher than the values reported in Table III. Torre *et al.* [44] performed an OKE experiment between 370 K and 290 K which should give the same information on the rotational dynamics as the VH backscattering experiment. Their τ_α values agree very well with the present measurement. More recently, Torre *et al.* [62] performed a polarized TG experiment. The heterodyne detected signal is sensitive to the polarization of the probe when both the density and the molecular orientation contribute to the modulation of the dielectric tensor [63]. The polarization effect they measure is in qualitative agreement with the existence of a sizeable VV dip, but a quantitative analysis of the experiment has not yet been performed.

B. Comparison of the VV dip and the Rytov dip

Finally, we consider the similarities and the differences between the VV dip and the well-known VH (or Rytov) dip.

TABLE III. Analysis of 90° VH salol spectra. The values in part *A* were obtained from the fits described in Sec. V A, those in part *D* from the fits described in Sec. V D, etc. The final two parts, *C*1 and *C*2, show the results of the two methods of fitting the low-temperature spectra discussed in Sec. V C. Parameters held constant in the fits are indicated by $*$

T (K)	$\eta_S(Pa.s)^*$ (Experiment)	q^2/ρ_{m^*} (10^9 m/kg)	Λ (10^7 Pa)			I_0	χ^2	
A. High-temperature fits			Λ	$\eta_S(Pa.s)$	δ	I_0	χ^2	
380	2.23×10^{-3}	639.6	1.56	2.65×10^{-3}	6.11×10^{3}	1.09×10^{6}	3.4	
370	2.46×10^{-3}	638.3	1.46	2.67×10^{-3}	1.50×10^{4}	1.07×10^{6}	7.9	
360	2.78×10^{-3}	637.1	1.42	3.06×10^{-3}	1.65×10^{4}	1.19×10^{6}	8.2	
350	3.22×10^{-3}	635.8	1.63	4.30×10^{-3}	1.38×10^{4}	1.13×10^{6}	2.4	
D. Interpolation region fits			Λ^*	β_S^*	$\tau_S(ns)^*$	I_0	χ^2	
340	3.85×10^{-3}	634.6	1.63	0.400	8.68×10^{-3}	1.170×10^{6}	0.89	
330	4.81×10^{-3}	633.4	1.63	0.390	1.18×10^{-2}	0.936×10^{6}	2.0	
320	6.41×10^{-3}	632.3	1.63	0.380	1.72×10^{-2}	1.082×10^{6}	3.4	
310	9.38×10^{-3}	631.1	1.63	0.375	2.76×10^{-2}	1.210×10^{6}	3.5	
300	1.58×10^{-2}	630.0	1.63	0.370	5.08×10^{-2}	1.140×10^{6}	15.8	
295	2.21×10^{-2}	629.5	1.63	0.360	7.37×10^{-2}	1.160×10^{6}	13.0	
290	3.31×10^{-2}	628.9	1.63	0.355	1.14×10^{-1}	1.290×10^{6}	24.0	
285	5.42×10^{-2}	628.4	1.63	0.350	1.88×10^{-1}	1.290×10^{6}	8.5	
B. Crossover region fits			Λ	β_S	$\tau_S(ns)$	I_0	χ^2	
280	9.91×10^{-2}	627.9	1.64	0.49	0.293	1.47×10^{6}	5.8	
275	2.09×10^{-1}	627.4	1.82	0.30	0.75	1.37×10^{6}	3.5	
270	5.24×10^{-1}	626.9	2.03	0.23	2.13	1.19×10^{6}	1.1	
265	1.63	626.4	2.22	0.21	6.91	1.20×10^{6}	2.3	
260	6.45	625.9	2.60	0.19	28.6	8.28×10^{5}	1.4	
255	3.35×10^{1}	625.4	2.60	0.18	157.0	8.22×10^{5}	2.2	
250	2.30×10^{2}	624.9	4.90	0.14	1.10×10^{3}	4.14×10^{5}	1.2	
*C*1. Low-temperature fits 1			Λ	β_S	$\tau_S(ns)$	I_0	χ^2	p_S
240	2.47×10^{4}	623.9	12.6	0.15^*	7.44×10^{4}	1.40×10^{5}	2.2	1.53×10^{-2}
230	7.35×10^{6}	623.0	19.1	0.15^*	1.78×10^{7}	6.00×10^{4}	4.9	1.49×10^{-2}
220	5.55×10^{9}	622.0	21.6	0.15^*	1.21×10^{10}	7.00×10^{4}	8.5	8.51×10^{-3}
210	1.04×10^{13}	621.1	17.2	0.15^*	2.49×10^{13}	9.00×10^{4}	6.1	2.12×10^{-3}
*C*2. Low-temperature fits 2			Λ	β_{S^*}	$\tau_S(ns)$	I_0	χ^2	$p_S=p_R$
240	2.47×10^{4}	623.9	7.7	0.15^*	9.15×10^{4}	2.50×10^{5}	4.9	1.50×10^{-3}
230	7.35×10^{6}	623.0	13.8	0.15^*	2.04×10^{7}	1.00×10^{5}	7.6	1.10×10^{-3}
220	5.55×10^{9}	622.0	17.7	0.15^*	1.32×10^{10}	1.00×10^{5}	21.0	6.00×10^{-4}
210	1.04×10^{13}	621.1	5.56	0.15^*	3.77×10^{13}	3.00×10^{5}	17.0	1.40×10^{-4}
			16.9	0.15^*				

For the present discussion, it is easier to concentrate on the difference spectra, i.e., spectra obtained by subtracting the scaled $I_{VH}^{back}(\omega)$ spectra from the full $I_{VV}^{90}(\vec{q},\omega)$ or $I_{VH}^{90}(\vec{q},\omega)$ spectra. Both dips are the consequence of the detection of excitations (longitudinal or transverse) via induced orientation of the molecules coupled to those excitations. Mathematically, these dips result from taking the $\omega\tau \ll 1$ limit of each relaxation function in the second term of Eqs. (45) or (36). It is easily shown that, at low temperature, the VV dip (when it exists—see below) and the VH dip have depths proportional to $\tau_B(\tau_S)$ and widths proportional to $\tau_B^{-1}(\tau_S^{-1})$, respectively. Consequently, at low temperature where $\omega_B\tau \ll 1$, the polarized and depolarized difference spectra have similar shapes. They both contain a propagating mode and a negative, deep, and narrow central dip. Note, however, that in the full VH spectrum, the increasing depth of the VH dip can be masked by the increasing strength of the orientational component. Thus, in Fig. 10, where each VH spectrum has been independently rescaled for clarity, the *relative* size of the dip appears to decrease with decreasing temperature although, when viewed on an absolute intensity scale, it actually increases.

The disappearance of the dips from the spectra with decreasing temperature is an experimental artefact due to limited resolution and/or parasitic scattering, but is not a consequence of the theory. If, however, it were possible to follow the VV dip to sufficiently low temperatures that its width became comparable to that of the thermal diffusion mode—

TABLE IV. Analysis of 90° VV salol spectra. The first column gives the scaling factor for matching the high-frequency $I_{VH}^{back}(\omega)$ spectra to the $I_{VV}^{90}(\vec{q},\omega)$ spectra described in Sec. VI A. The second column gives I_0 obtained from the high-frequency fits described in Sec. V B. Columns 3–5 are the results of the preliminary damped oscillator fits [Eq. (50)], used to obtain ω_B and Γ_B values. The next two columns give the resulting values of $\omega_B\tau_R$ and $\omega_B\tau_S$. The last three columns give the results of the full fits described in Sec. VI B.

T (K)	I_{VH}-back scaling	Hi-ω-fit I_0	Damped oscil. fit to peak Fit range	$\omega_B/2\pi$	$\Gamma_B/2\pi$	$\omega_B^*\tau_R$	$\omega_B^*\tau_S$	Full fits ($\Gamma_0=T/600$) $\omega_0/2\pi$	S	V
380	0.158	9.456×10^5	4.76−5.90	5.41	0.94	2.09	0.12	5.36	7.4133	1.4201
370	0.179	1.016×10^6	4.9−6.04	5.57	1.04	2.60	0.15	5.51	7.473	1.6866
360	0.17	1.044×10^6	5.1−6.2	5.73	1.09	3.29	0.19	5.66	7.3476	1.7455
350	0.165	9.644×10^5	5.2−6.35	5.92	1.23	4.23	0.25	5.83	6.9711	2.0654
340	0.175	1.014×10^6	5.4−6.6	6.13	1.31	5.65	0.33	6.02	7.014	2.1991
330	0.155	9.426×10^5	5.6−7	6.46	1.5	7.94	0.47	6.28	6.8972	2.3389
320	0.162	9.440×10^5	6−7.15	6.75	1.65	12.15	0.73	6.47	6.8521	2.2903
310	0.173	1.009×10^6	6.2−7.6	7.09	1.7	20.67	1.23	6.63	6.6691	2.2025
300	0.166	1.049×10^6	6.6−8	7.49	1.66	39.81	2.39	6.77	6.5604	2.2587
290	0.15	1.056×10^6	7.2−8.35	7.9	1.5	93.81	5.66	6.92	6.106	2.3093
280	0.174	1.103×10^6	7.4−9	8.3	1.21	2.95×10^2	15.28	7.1	6.0511	1.9717
270	0.167	9.943×10^5	8.1−9.22	8.72	0.967	1.42×10^3	1.17×10^2	7.18	5.7227	2.3023
260	0.178	9.412×10^5	8.6−9.5	9.13	0.769	1.30×10^4	1.64×10^3	7.51	5.0262	2.2171
250	0.214	4.501×10^5	9.1−9.9	9.52	0.625	2.92×10^5	6.04×10^4	7.79	5.2356	2.0612
240	0.218	1.787×10^5	9.5−10.3	9.93	0.52	2.08×10^7	4.64×10^6	8.1	5.1025	1.6797

which is not included in our analysis—then it might disappear.

There is, however, a fundamental difference between the two dips in that the VH dip always exists (although it may be too weak to detect for small molecular anisotropy) while this is not always the case for the VV dip. The sign of $I_{dif}(\vec{q},\omega)$ at $\omega\sim0$ is determined by the square bracket on the right-hand-side of Eq. (57): $\left[(S/\rho_m)-\frac{4}{3}(\omega_0/q)^2R_0\beta_R(\tau_R/\eta_L)\right]$ which does not depend on q and depends only weakly on temperature. Its first part represents the Mountain mode detected (up to a scaling factor) by the density fluctuations. The second part always decreases the corresponding intensity but reverses its sign (creates a dip) only for small enough values of S, i.e., when the change of polarizability due to molecular orientation is large enough to counterbalance the role of the density fluctuations. (Recall that $S\propto a/b$). The appearance of the VV dip therefore requires that the ratio of b/a, the two optical coupling constants in Eq. (9), exceed a material-dependent minimum value. This is the case for salol, but it is certainly not a general rule. If the molecules are not sufficiently anisotropic, there will be no VV dip.

ACKNOWLEDGMENTS

We thank W. Götze, T. Franosch, C. Dreyfus, M. Fuchs, and C. H. Wang for helpful discussions, B. Bonello for providing the ultrasonic data used to find C_0, G. Hinze for the OKE data, and E. W. Fischer for providing the dielectric data from Ref. [42]. This material is based upon work supported by the National Science Foundation under Grant Nos. DMR-9980370 and DMR-0243471.

APPENDIX: DETERMINATION OF THE ORIENTATIONAL AMPLITUDE FACTOR R_0

The spectrum of pure orientational fluctuations, measured in depolarized backscattering, is given by Eq. (25):

$$I_{VH}^{back}(\omega)=\frac{I_0}{\omega}\mathrm{Im}[R(\omega)], \tag{A1}$$

where $1/\omega R(\omega)=i\int_0^\infty e^{-i\omega t}\phi_Q(t)dt$ is the Laplace transform of the normalized orientational correlation function $\phi_Q(t)$. In the data analysis, we model $R(\omega)$ with the "hybrid function" [Eq. (37)] which combines the Cole-Davidson function for the α decay with a high-frequency power-law term:

$$\begin{aligned}R(\omega)&=R_0H_R(\omega)\\&=R_0\{[1-(1+i\omega\tau)^{-\beta}]+p[(i\omega)(\tau^{-1}-i\omega)^{a-1}]\}.\end{aligned} \tag{A2}$$

In order to avoid having the amplitude factor R_0 as a free fitting parameter, we carried out a separate determination of its value.

The normalized orientational spectrum $S_R(\omega)$ [with $\int_{-\infty}^{\infty}S_R(\omega)d\omega=1$] is given by

$$S_R(\omega)=\frac{1}{\pi}\mathrm{Re}\int_0^\infty e^{-i\omega t}\phi_Q(t)dt \tag{A3}$$

so that $S_R(\omega)=(1/\pi\omega)\mathrm{Im}[R(\omega)]$. The CD part of the normalized spectrum is therefore $S_{CD}(\omega)=(R_0/\pi\omega)\times[1-(1+i\omega\tau_{CD})^{-\beta_{CD}}]$ with the low-frequency limit:

$$S_{CD}(\omega\to0)=R_0\beta_{CD}\tau_{CD}/\pi. \tag{A4}$$

The normalized orientational correlation function $\phi_Q(t)$ begins at $\phi_Q(t=0)=1$. After the initial fast decay to a plateau level $f_K \leqslant 1$ (approximately the nonergodicity parameter of MCT), the long-time α-decay region can be fit with the KWW stretched exponential function:

$$\phi_K(t) = f_K e^{-(t/\tau_K)^{\beta_K}}. \quad \text{(A5)}$$

The α-relaxation part of the corresponding normalized spectrum is therefore given, in the low-frequency limit, by

$$S_K(\omega \to 0) = \frac{1}{\pi}\int_0^\infty f_K e^{-(t/\tau_K)^{\beta_K}} dt = \frac{f_K \tau_K}{\pi \beta_K}\Gamma\left(\frac{1}{\beta_K}\right). \quad \text{(A6)}$$

Since $S_{CD}(\omega)$ and $S_K(\omega)$ should correspond to the same α-relaxation spectrum, we can equate the two $\omega \to 0$ values of Eqs. (A4) and (A6), which then gives

$$R_o = \left(f_K \frac{\tau_K}{\tau_{CD}\beta_K\beta_{CD}}\right)\Gamma\left(\frac{1}{\beta_K}\right). \quad \text{(A7)}$$

We analyzed the high-temperature $I_{VH}^{back}(\omega)$ spectra using the hybrid model, which gave β_{CD} and τ_{CD}. Also, since the integrated α-relaxation spectrum is given by $\int_0^\infty S_K(\omega)d\omega = f_K/2$, we integrated both the CD fit to the α-relaxation spectrum $[I_\alpha(\omega)]$ and the full experimental spectrum $I(\omega)$ to obtain f_K:

$$f_K = \frac{\displaystyle\int_0^\infty I_\alpha(\omega)d\omega}{\displaystyle\int_0^\infty I(\omega)d\omega}. \quad \text{(A8)}$$

Our hybrid model fits to the highest temperatures gave $\beta_{CD}=0.78$, so that, from Eq. (A7), $R_o(\beta_{CD}=0.78)=1.03 f_K$ where we used the prescription of Lindsey and Patterson [39] to relate β_K to β_{CD} and τ_K to τ_{CD}. At high temperatures, Eq. (A8) gave $f_K \simeq 0.88$ so that, from Eq. (A7), $R_o = 1.03 f_K \simeq 0.90$. A similar value for R_o was found from the f_K values obtained in KWW fits to the low-temperature PCS data (see Sec. III C). The value of R_0 was therefore fixed at 0.9 in the analyses of the spectra for all temperatures.

[1] V. S. Starunov, E. V. Tiganov, and I. L. Fabelinskii, Pis'ma Zh. Eksp. Teor. Fiz. **5**, 317 (1967) [JETP Lett. **5**, 260 (1967)].

[2] I. L. Fabelinskii, L. M. Sabirov, and V. S. Starunov, Phys. Lett. **29A**, 414 (1969).

[3] L. M. Sabirov, V. S. Starunov, and I. L. Fabelinskii, Zh. Eksp. Teor. Fiz. **60**, 146 (1971) [Sov. Phys. JETP **33**, 82 (1971)].

[4] V. S. Starunov and I. L. Fabelinskii, Zh. Eksp. Teor. Fiz. **66**, 1740 (1974) [Sov. Phys. JETP **39**, 854 (1974)].

[5] G. I. A. Stegeman and B. P. Stoicheff, Phys. Rev. Lett. **21**, 202 (1968); Phys. Rev. A **7**, 1160 (1973).

[6] G. D. Enright, G. I. A. Stegeman, and B. P. Stoicheff, J. Phys. (Paris) **33**, C1-207 (1972).

[7] G. D. Enright and B. P. Stoicheff, J. Chem. Phys. **64**, 3658 (1976).

[8] M. Leontovich, Izv. Akad. Nauk SSSR, Ser. Fiz. **5**, 148 (1941) [J. Phys. (USSR) **4**, 499 (1941)]; Bull. Acad. Sci. USSR, Phys. Ser. (Engl. Transl.) **4**, 499 (1941).

[9] S. M. Rytov, Zh. Eksp. Teor. Fiz. **33**, 514 (1957); **33**, 669 (1957) [Sov. Phys. JETP **6**, 401 (1958); **6**, 513 (1958)].

[10] C. Tanford, *Physical Chemistry of Macromolecules* (Wiley, New York, 1961), p. 436.

[11] H. C. Andersen and R. Pecora, J. Chem. Phys. **54**, 2584 (1971); **55**, 1496 (1972).

[12] T. Keyes and D. Kivelson, J. Chem. Phys. **54**, 1786 (1971); T. Keyes and D. Kivelson, J. Phys. (Paris) **33**, C1-231 (1972); T. Keyes and D. Kivelson, J. Chem. Phys. **56**, 1876 (1972).

[13] C. H. Wang, Mol. Phys. **41**, 541 (1980).

[14] W. Lempert and C. H. Wang, J. Chem. Phys. **76**, 1283 (1982).

[15] C. H. Wang and Q.-L. Liu, J. Chem. Phys. **78**, 4363 (1983).

[16] C. H. Wang, R. J. Ma, G. Fytas, and Th. Dorfmuller, J. Chem. Phys. **78**, 5863 (1983).

[17] C. H. Wang and J. Zhang, J. Chem. Phys. **85**, 794 (1986).

[18] C. H. Wang, X. R. Zhu, and J. C. Shen, Mol. Phys. **62**, 749 (1987).

[19] C. H. Wang, Mol. Phys. **58**, 497 (1986).

[20] C. Dreyfus, A. Aouadi, R. M. Pick, T. Berger, A. Patkowski, and W. Steffen, Europhys. Lett. **42**, 55 (1998); J. Phys.: Condens. Matter **11**, A139 (1999).

[21] C. Dreyfus, A. Aouadi, R. M. Pick, T. Berger, A. Patkowski, and W. Steffen, Eur. Phys. J. B **9**, 401 (1999).

[22] C. Dreyfus and R. M. Pick (unpublished).

[23] C. Dreyfus, A. Aouadi, J. Gapinski, M. Matos-Lopez, W. Steffen, A. Patkowski, and R. M. Pick, Phys. Rev. E **68**, 011204 (2003).

[24] G. Monaco *et al.* (unpublished).

[25] P. J. Chappell and D. Kivelson, J. Chem. Phys. **76**, 1742 (1982).

[26] R. M. Pick, T. Franosch, A. Latz, and C. Dreyfus, Eur. Phys. J. B **31**, 217 (2003).

[27] T. Franosch, A. Latz, and R. M. Pick, Eur. Phys. J. B **31**, 229 (2003).

[28] H. P. Zhang, A. Brodin, H. C. Barshilia, G. Q. Shen, H. Z. Cummins, and R. M. Pick (unpublished).

[29] W. Götze and L. Sjögren, Rep. Prog. Phys. **55**, 241 (1992).

[30] R. D. Mountain, Rev. Mod. Phys. **38**, 205 (1966).

[31] B. J. Berne and R. Pecora, *Dynamic Light Scattering* (Wiley, New York, 1976) (reprinted by Dover Publications, 2000).

[32] T. Franosch, M. Fuchs, and A. Latz, Phys. Rev. E **63**, 061209 (2001).

[33] A. Latz and M. Letz, Eur. Phys. J. B **19**, 323 (2001).

[34] M. G. Schultz, Diploma thesis, Freie Universitat Berlin, 2003; M. G. Schultz and T. Franosch (unpublished).

[35] G. Li, W. M. Du, A. Sakai, and H. Z. Cummins, Phys. Rev. A **46**, 3343 (1992).

[36] C. Vaucamps, J. P. Chabrat, L. Letamendia, G. Nouchi, and J. Rouch, Opt. Commun. **15**, 201 (1975).

[37] C. Dreyfus, M. J. Lebon, H. Z. Cummins, J. Toulouse, B. Bonello, and R. M. Pick, Phys. Rev. Lett. **69**, 3666 (1992); **76**, 1763 (1996).

[38] H. Z. Cummins, G. Li, W. M. Du, R. M. Pick, and C. Dreyfus, Phys. Rev. E **53**, 896 (1996); **55**, 1232 (1997).

[39] C. P. Lindsey and G. D. Patterson, J. Chem. Phys. **73**, 3348 (1980).

[40] M. H. Cohen and G. S. Grest, J. Non-Cryst. Solids **61-62**, 749 (1984); G. S. Grest and M. H. Cohen, Adv. Chem. Phys. **48**, 455 (1981).

[41] P. K. Dixon, L. Wu, S. R. Nagel, B. D. Williams, and J. P. Carini, Phys. Rev. Lett. **65**, 1108 (1990).

[42] F. Stickel, E. W. Fischer, and R. Richert, J. Chem. Phys. **102** 6251 (1995).

[43] D. L. Sidebottom and C. M. Sorenson, Phys. Rev. B **40** 461 (1989).

[44] R. Torre, P. Bartolini, and R. M. Pick, Phys. Rev. E **57**, 1912 (1998).

[45] W. Götze, A. P. Singh, and Th. Voigtmann, Phys. Rev. E **61**, 6934 (2000); S. H. Chong and W. Götze, Phys. Rev. E **65**, 041503 (2002); **65**, 051201, (2002).

[46] V. O. Jantsch, Z. Kristallogr. **108**, 185 (1956).

[47] W. T. Laughlin and D. R. Uhlmann, J. Phys. Chem. **76**, 2317 (1972).

[48] M. Cukierman, J. W. Lane, and D. R. Uhlmann, J. Chem. Phys. **59**, 3639 (1973).

[49] A. Brodin, M. Frank, S. Wiebel, G. Shen, J. Wuttke, and H. Z. Cummins, Phys. Rev. E **65**, 051503 (2002).

[50] J. Wiedersich, N. V. Surovtsev, and E. Rossler, J. Chem. Phys. **113**, 1143 (2000).

[51] S. V. Adichtev, St. Benkhof, Th. Blochowitz, V. N. Novikov, E. Rossler, Ch. Tschirwitz, and J. Wiedersich, Phys. Rev. Lett. **88**, 055703 (2002).

[52] M. D. Ediger, Annu. Rev. Phys. Chem. **51**, 99 (2000).

[53] G. Hinze, D. B. Brace, S. D. Gottke, and M. D. Fayer, J. Chem. Phys. **113**, 3723 (2000).

[54] G. Hinze (private communication).

[55] Hu Cang, V. N. Novikov, and M. D. Fayer, Phys. Rev. Lett. **90**, 197401 (2003); J. Chem. Phys. **118**, 2800 (2003).

[56] J. Wiedersich (private communication).

[57] C. Dreyfus, M. J. Lebon, F. Vivicorsi, A. Aouadi, R. M. Pick, and H. Z. Cummins, Phys. Rev. E **63**, 041509 (2001).

[58] B. Bonello and J. Toulouse (unpublished).

[59] W. Götze and M. Sperl, Phys. Rev. Lett. **92**, 105701 (2004); M. Ricci, S. Wiebel, P. Bartolini, A. Taschin, and R. Torre, Philos. Mag. (to be published).

[60] I. Chang and H. Sillescu, J. Phys. Chem. B **101**, 8794 (1997).

[61] Y. Yang and K. Nelson, J. Chem. Phys. **103**, 7732 (1995).

[62] A. Taschin, P. Bartolini, M. Ricci, and R. Torre, in *Proceedings of the XII UPS Conference, Florence, 2001: Recent Advances in Ultrafast Spectroscopy*, edited by S. Califano, P. Foggi, and R. Righini (Leo S. Olschki, Firenze, 2003), p. 349.

[63] A. Taschin, R. Torre, M. Ricci, M. Sampoli, C. Dreyfus, and R. M. Pick, Europhys. Lett. **56**, 407 (2001); R. M. Pick, C. Dreyfus, A. Azzimani, A. Taschin, M. Ricci, R. Torre, and T. Franosch, J. Phys.: Condens. Matter **15**, S825 (2003).

[64] Y. Yang and K. A. Nelson, Phys. Rev. Lett. **74**, 4883 (1995).

[65] H. Z. Cummins, W. M. Du, M. Fuchs, W. Gotze, S. Hildebrand, A. Latz, G. Li, and N. J. Tao, Phys. Rev. E **47**, 4223 (1993).